

Dynamical Low-Rank Ensemble Kalman filter for State/Parameter estimation

Fabio Nobile¹, Sébastien Riffaud¹, and Thomas Trigo Trindade¹

¹Institute of Mathematics, École Polytechnique Fédérale de Lausanne, 1015 Lausanne,
Switzerland

{fabio.nobile,sebastien.riffaud,thomas.trigotrindade}@epfl.ch

Abstract

We propose a Dynamical Low-Rank Ensemble Kalman Filter (DLR-ENKF) for efficient joint state-parameter estimation in high-dimensional dynamical systems. The method extends the DLR-ENKF formulation of [29] to the augmented state-parameter framework, tracking the filtering density within a dynamically evolving low-dimensional subspace. Key developments include a time-integration strategy that combines the Basis Update & Galerkin scheme with forecast/analysis discretisation, and a DEIM-based hyper-reduction technique for efficient evaluation of nonlinear terms. We demonstrate the effectiveness, robustness, and computational advantages of the proposed approach on benchmark problems. The results highlight the potential of dynamically evolving reduced bases to achieve accurate filtering and parameter estimation at reduced computational cost.

Keywords: Ensemble Kalman Filtering, Parameter identification, Dynamical Low-Rank Approximation, Discrete Empirical Interpolation Method, Basis Update & Galerkin integrator

1 Introduction

In Uncertainty Quantification, state and/or parameter identification tasks remain challenging due to their high computational cost. This work focuses on the Bayesian data assimilation framework, where a signal $\mathcal{X}_t^{\text{true}}$ evolves according to model dynamics that depend on an unknown parameter θ^{true} . The signal is observed through an observation process \mathcal{Z}_t , defined as a (linear) functional of the signal and perturbed by additive noise. The Bayesian problem consists in characterising the posterior density of $(\mathcal{X}_t, \theta_t)$ conditional on the observations. In filtering, this posterior is updated sequentially using incoming data, together with the current distributions of the state and parameters. Since the exact filtering density is not available in closed form, approximate methods are required. Common approaches include particle-based techniques such as Sequential Monte Carlo (particle filters) and ensemble-based methods such as the Ensemble Kalman Filter (ENKF). However, when the state dynamics is high-dimensional – for instance, arising from the fine discretisation of a time-dependent PDE – the computational cost of propagating the dynamical system can become prohibitive for a large number of particles.

Ensemble Kalman methods are known to achieve effective signal tracking even with a moderate number of particles – unlike Sequential Monte Carlo methods, which are prone to particle collapse. This suggests the existence of a low-rank “filtering subspace”, i.e., the filtering density concentrates around a low-dimensional subspace. However, the ENKF does not explicitly exploit this low-rank structure: the cost of propagating particles still scales with the full state-space dimension, rather than the reduced dimension of the subspace. The work [29] addresses this issue by developing a framework that evolves a low-dimensional filtering subspace using the Dynamical Low-Rank (DLR) approximation method. Originally

introduced for matrix differential equations [19], DLR approximations propagate a low-rank, SVD-like representation of the solution through tailored time-integration schemes [6, 25], thereby avoiding repeated costly SVD truncations at each step. The method has also been applied in Uncertainty Quantification for random PDEs [15, 27, 34] and SDEs [16]. The objective of this work is to design a practical DLR-ENKF algorithm for efficient joint state-parameter estimation in the context of time-continuous observations. To this end, we extend the formulation of [29] to nonlinear dynamical systems and further investigate several questions left open in that work, which are crucial for robust and efficient propagation of the low-rank system. In particular, we examine the development of suitable time-integration schemes and the use of hyper-reduction techniques for efficient treatment of nonlinear terms. These aspects will be central to the approach presented in this paper.

The main contributions of this paper are the following. First, we adapt the DLR-ENKF formulation of [29] to nonlinear dynamics and the augmented-state ENKF framework in order to perform joint state-parameter estimation [1, 30]. Second, we propose a time-integration strategy that combines the Basis Update & Galerkin scheme [5] with the forecast/analysis-based discretisation. Third, we introduce a novel DEIM-based approach to accelerate the evaluation of nonlinear terms. Finally, we demonstrate the effectiveness, strengths, and limitations of the method through applications to representative model problems.

This work lies within the broader research area that studies the integration of reduced basis methods into state and/or parameter identification problems. Closely related to our problem setting, [31] combines the POD Reduced Basis technique with an augmented-state ENKF formulation, supplemented by a Reduced Error Model to mitigate the biases introduced by the model order reduction. Fixed reduced basis methods may not perform well when the ensemble of solutions does not exhibit a low-rank profile globally in space and time. This limitation is particularly evident in problems with traveling wave fronts: although the solution may admit a low-rank representation at each fixed time, its global-in-time evolution is not well captured by a fixed spatial basis. Additionally, fixed reduced basis methods rely on an offline procedure, in which solution snapshots are sampled using the full order model to learn the solution manifold, which can be computationally prohibitive for problems involving a large number of parameters. Since the reduced basis is learnt before observing the system, it must be sufficiently large to be able to track effectively the signal in the online phase. In contrast, our approach does not require an offline procedure and employs a reduced basis that evolves dynamically in time, enabling more efficient tracking of the filtering density with a significantly smaller basis.

Several other works have explored the integration of dynamic reduced basis techniques in data assimilation, specifically in the context of discrete time observations. For instance, [39] proposes an adaptive technique to update the reduced basis in the online phase in the context of multi-fidelity/level Ensemble Kalman filters. More closely related to our setting, a number of works specifically employ dynamical low-rank techniques. One example is the blended particle filters framework [26], which builds on the (modified) quasilinear Gaussian-DO method [36, 35] to perform data assimilation of chaotic large-scale systems (with an emphasis on handling non-Gaussian features). Finally, the authors in [41, 40] use DLR techniques to accelerate the forecast step and fit the forecasted particles to a Gaussian mixture model for the assimilation step.

We also mention related work in the broader context of Bayesian parameter identification for parametrised, time-dependent PDEs: [32] develops a low-rank MCMC method that exploits dynamically evolving low-rank bases to reduce computational costs while maintaining accuracy. Alternatively, [38] proposes surrogate models for Ensemble Kalman Inversion (EKI), combined with reduced-order model (ROM) bias correction. While the former relies on an MCMC method based on low-rank approximations and the latter follows a ROM-based Ensemble Kalman Inversion approach, both methods do not assimilate observations sequentially and are designed for smoothing problems. In contrast, our method assimilates data on-the-fly, which makes it naturally suited for filtering applications.

The paper is organised as follows. Section 2 introduces the concepts and notation for the filtering problem. In Section 3, we present the DLR-ENKF equations for parameter identification, together with the proposed time-integration scheme and its DEIM-based acceleration. In Section 4, we assess the efficiency of the method on two parameter identification problems, a Fisher-KPP model and a blood flow model.

2 Problem setting

Let $(\Omega, \mathcal{A}, \mathbb{P}; (\mathcal{A}_t)_{t \geq 0})$ be a complete right-continuous filtered probability space. Denote by $\text{Mat}(m \times n)$ the set of real-valued $m \times n$ matrices, and $\text{Mat}_+(m)$, resp. $\text{Mat}_0(m)$, the set of symmetric positive resp. semi-positive-definite $m \times m$ matrices. For $A \in \text{Mat}(m \times n)$, denote $\|A\|_F^2 = \text{tr}(A^\top A)$ the Frobenius norm, and by $\mathcal{T}_R(A) \in \text{argmin}\{\|A - B\|_F, \text{rank}(B) \leq R\}$ a best rank- R approximation of A , which is unique if the R -th singular value $\sigma_R(A)$ is strictly larger than the following one $\sigma_{R+1}(A)$.

We consider a system whose state $\mathcal{X}_t^{\text{true}} \in \mathbb{R}^d$ (hereafter called the signal) evolves according to some parameter-dependent *true dynamics*

$$d\mathcal{X}_t^{\text{true}} = f(\mathcal{X}_t^{\text{true}}, \theta^{\text{true}})dt, \quad t \geq 0, \quad (1)$$

with $f : \mathbb{R}^d \rightarrow \mathbb{R}^d$. The dynamics depend on the *true parameter* vector $\theta^{\text{true}} \in \mathbb{R}^{n_\theta}$, which will be assumed to have a small to moderate dimension. The signal is partially observed via the process $\mathcal{Z}_t \in \mathbb{R}^k$ where $k < d$, driven by

$$d\mathcal{Z}_t = H\mathcal{X}_t^{\text{true}}dt + \Gamma^{1/2}d\tilde{\mathcal{V}}_t. \quad (2)$$

with $H \in \text{Mat}(k \times d)$ a *linear observation operator* and $\Gamma \in \text{Mat}_+(k)$, and where $\tilde{\mathcal{V}}_t$ is a k -dimensional \mathcal{A}_t -adapted Brownian motion. We set $\mathcal{Z}_0 = \mathbf{0} \in \mathbb{R}^k$ and denote $\mathcal{A}_{\mathcal{Z}_t} = \sigma(\mathcal{Z}_s, 0 \leq s \leq t)$ the sub- σ -algebra generated by the observations up to time t , in other words the history of observations, whereas $f_t^* = f - \mathbb{E}[f | \mathcal{A}_{\mathcal{Z}_t}]$ denotes the zero conditional mean part of f . For $f \in L^1(\Omega)$, the conditional expectation taken with respect to $\mathcal{A}_{\mathcal{Z}_t}$ shall be denoted by $\mathbb{E}[f | \mathcal{A}_{\mathcal{Z}_t}]$.

In this work, we consider the situation where $\mathcal{X}_0^{\text{true}}$ and θ^{true} are unknown, and use a Bayesian approach to infer the true state and parameter from the data. To this end, we model $\mathcal{X}_0^{\text{true}}$ and θ^{true} as random variables, with prior distribution $(\mathcal{X}_0, \theta_0) \sim \pi_{\text{pr}}$. Then, we aim to efficiently approximate the state distribution at any time $t \geq 0$ conditional on the data $\text{Law}(\mathcal{X}_t^{\text{true}} | \mathcal{A}_{\mathcal{Z}_t})$ as well as the parameter distribution $\text{Law}(\theta^{\text{true}} | \mathcal{A}_{\mathcal{Z}_t})$. We propose to do this by following an Ensemble Kalman Filter approach [3]. The setup is similar to the one of Ensemble Kalman Inversion [37], with the difference that the observation process varies in time and is assimilated on the fly. We refer to [30] for a discussion on the Ensemble Kalman filter for state/parameter estimation in the context of time-varying observations.

The approach proceeds by (a) constructing an augmented state process $(\mathcal{X}_t^{\text{true}}, \theta_t^{\text{true}}) \equiv \bar{\mathcal{X}}_t \in \mathbb{R}^{d+n_\theta}$, and (b) applying the Kalman equations to the augmented state dynamics, which verifies

$$d\bar{\mathcal{X}}_t^{\text{true}} = \bar{f}(\bar{\mathcal{X}}_t^{\text{true}})dt, \quad t \geq 0, \quad \bar{\mathcal{X}}_0^{\text{true}} = (\mathcal{X}_0^{\text{true}}, \theta_0^{\text{true}}) \quad (3)$$

where $\bar{f}(\bar{\mathcal{X}}_t^{\text{true}}) = [f(\mathcal{X}_t^{\text{true}}, \theta_t^{\text{true}}), \mathbf{0}_{n_\theta}]^\top$, and observation process

$$d\mathcal{Z}_t = \bar{H}\bar{\mathcal{X}}_t^{\text{true}}dt + \Gamma^{1/2}d\tilde{\mathcal{V}}_t, \quad (4)$$

where $\bar{H} = [H, \mathbf{0}_{k \times n_\theta}]$. Note that in the augmented dynamics, $d\theta_t^{\text{true}} = 0$ with $\theta_0^{\text{true}} = \theta^{\text{true}}$, and therefore the augmented dynamics and observations is equivalent to the original dynamics and observations. As $\mathcal{X}_0^{\text{true}}$ and θ_0^{true} are random (and distributed according to π_{pr}), the Kalman filter will induce a non-trivial dynamics on the parameter θ_t , which hopefully will approach θ^{true} if the observation process is sufficiently informative.

2.1 Augmented State Kalman filtering

Ensemble Kalman filters are equal-weight interacting particle systems that evolve an empirical measure by combining the model dynamics with a corrective term depending on the observation process. Even when used with a moderate number of particles, these methods are less susceptible than standard particle filters to ensemble collapse [33], making these methods especially popular in large-scale data assimilation applications such as geosciences. The state/parameter identification equations are derived by applying the ENKF equations to the augmented state system (3) and (4). We refer to e.g. [30] for the construction in the filtering context (with model noise), or more broadly [14] for the derivation in the related Ensemble Kalman Inversion (EKI) context. We shall focus on two variants of the

ENKF, which, following the nomenclature in [3], are referred to as the Vanilla Ensemble Kalman filter (VENKF) and the Deterministic Ensemble Kalman filter (DENKF). Denote $\widehat{\mathcal{X}}_t = [\widehat{\mathcal{X}}_t^{(1)}, \dots, \widehat{\mathcal{X}}_t^{(P)}]$ a set of P augmented particles, and let

$$\begin{bmatrix} \widehat{m}_t^x \\ \widehat{m}_t^\theta \end{bmatrix} = \widehat{m}_t = \widehat{m}_t(\widehat{\mathcal{X}}_t) = \mathbb{E}_P[\widehat{\mathcal{X}}_t] := \frac{1}{P} \sum_{i=1}^P \widehat{\mathcal{X}}_t^{(i)}, \quad \widehat{\mathcal{X}}_t^* = \widehat{\mathcal{X}}_t - \mathbb{E}_P[\widehat{\mathcal{X}}_t],$$

be the sample mean and the sample zero-mean ensemble, respectively, and

$$\widehat{P}_t = \widehat{P}_t(\widehat{\mathcal{X}}_t) = \frac{P}{P-1} \mathbb{E}_P[\widehat{\mathcal{X}}_t^* (\widehat{\mathcal{X}}_t^*)^\top] = \begin{bmatrix} \widehat{P}_t^{xx} & \widehat{P}_t^{x\theta} \\ \widehat{P}_t^{\theta x} & \widehat{P}_t^{\theta\theta} \end{bmatrix}$$

the sample covariance. Furthermore, $\widehat{\mathcal{V}}_t = \{\widehat{\mathcal{V}}_t^{(p)}\}_{p=1}^P$ denotes an i.i.d sample of copies of \mathcal{V}_t . The Ensemble Kalman filters are then written as

$$\begin{aligned} d\widehat{\mathcal{X}}_t^{(p)} &= f(\widehat{\mathcal{X}}_t^{(p)}, \widehat{\theta}_t^{(p)}) dt \\ &\quad + \widehat{P}_t^{xx} H^\top \Gamma^{-1} \left(d\mathcal{Z}_t - \frac{1+\kappa}{2} H \widehat{\mathcal{X}}_t^{(p)} dt - \kappa \Gamma^{1/2} d\widehat{\mathcal{V}}_t^{(p)} - \frac{1-\kappa}{2} H \widehat{m}_t^x dt \right), \end{aligned} \quad (5)$$

$$d\widehat{\theta}_t^{(p)} = \widehat{P}_t^{\theta x} H^\top \Gamma^{-1} \left(d\mathcal{Z}_t - \frac{1+\kappa}{2} H \widehat{\mathcal{X}}_t^{(p)} dt - \kappa \Gamma^{1/2} d\widehat{\mathcal{V}}_t^{(p)} - \frac{1-\kappa}{2} H \widehat{m}_t^x dt \right), \quad (6)$$

where $\kappa = 1$ corresponds to the VENKF and $\kappa = 0$ to the DENKF. Observe that the VENKF mimicks the dynamics and observation process by adding a synthetic noise to the observation of the state; on the other hand, the DENKF has a more consensus-based interpretation, taking the difference between a given particle and the sample average. While computationally expensive, simulating the ENKF system (5) and (6) with a large number of particles is of interest for several reasons. In the asymptotic limit, the filter may converge to a given mean-field limit (if it exists); in particular, when applied to linear-affine dynamics, the mean-field limit of the Ensemble Kalman filter coincides with the true filtering distribution [8]. This ceases to be true when applying the ENKF equation to nonlinear dynamics, and the ENKF may then rather be understood as a dynamic state/parameter estimation method. We refer to [3] and references therein for a more detailed discussion on this topic. In any case, a higher number of particles is expected to improve the signal-tracking abilities of the filter.

Remark 2.1. *Anticipating the DLR-ENKF construction, the mean-field version of eqs. (5) and (6) will be of interest. Proceeding formally, it is assumed that the empirical measure $\widehat{\mu}_t^P = P^{-1} \sum_{i=1}^P \delta_{\widehat{\mathcal{X}}_t^{(i)}}$ converges (in some sense) to the mean-field distribution $\bar{\mu}_t$, and denote $\overline{\mathcal{X}}_t \sim \bar{\mu}_t$ its associated mean-field process. Then, the sample covariance \widehat{P}_t converges to $P_t = \mathbb{E}[\overline{\mathcal{X}}_t \overline{\mathcal{X}}_t^\top]$ (in some sense), and gives rise to the following (McKean-Vlasov) equations*

$$\begin{aligned} d\mathcal{X}_t &= f(\mathcal{X}_t, \theta_t) dt \\ &\quad + P_t^{xx} H^\top \Gamma^{-1} \left(d\mathcal{Z}_t - \frac{1+\kappa}{2} H \mathcal{X}_t dt - \kappa \Gamma^{1/2} d\mathcal{V}_t - \frac{1-\kappa}{2} H \mathbb{E}[\mathcal{X}_t | \mathcal{A}_{\mathcal{Z}_t}] dt \right), \end{aligned} \quad (7)$$

$$d\theta_t = P_t^{\theta x} H^\top \Gamma^{-1} \left(d\mathcal{Z}_t - \frac{1+\kappa}{2} H \mathcal{X}_t dt - \kappa \Gamma^{1/2} d\mathcal{V}_t - \frac{1-\kappa}{2} H \mathbb{E}[\mathcal{X}_t | \mathcal{A}_{\mathcal{Z}_t}] dt \right). \quad (8)$$

In the case of linear-affine dynamics, eq. (7) is known as a Kalman-Bucy process [3].

2.2 Time-discretisation schemes

The numerical discretisation of eqs. (5) and (6) may be performed in various fashions. A straightforward approach is to resort to standard SDE discretisations (Euler-Maruyama scheme or higher order methods [18]). Note that a special care must be taken, as explicit discretisations as the Euler-Maruyama method may not be stable owing to the nonlinear (non-uniformly Lipschitz) terms [13]. Furthermore, the above system can become stiff in

the case of small observation noise ($\|\Gamma\|_F \ll 1$), adding a potential source of numerical instability.

Alternatively, the update may mimic the forecast/analysis procedure typically encountered in the discrete time data assimilation setting. In essence, it inverts the steps taken in [17] to recover the continuous-time formulation starting from the discrete setting, and can be viewed as a semi-implicit splitting of the dynamics. It is in particular known that for a one-dimensional toy model mimicking the Kalman-Bucy filter, the scheme is strongly convergent [4]. The present work focuses on this latter approach, and we outline the steps of that development here.

On an interval $[t_0, t_1]$, the *forecast* step consists in evolving each particle following the model dynamics

$$\begin{aligned} d\hat{\mathcal{X}}_t^{f,(p)} &= f(\hat{\mathcal{X}}_t^{f,(p)}, \hat{\theta}_t^{f,(p)}) dt & \hat{\mathcal{X}}_{t_0}^{f,(p)} &= \hat{\mathcal{X}}_{t_0}^{(p)} \\ d\hat{\theta}_t^{f,(p)} &= 0, & \hat{\theta}_{t_0}^{f,(p)} &= \hat{\theta}_{t_0}^{(p)} \end{aligned} \quad (9)$$

via e.g. an Euler step, and then *analyse* the particles by subjecting them to the corrective dynamics

$$d \begin{bmatrix} \hat{\mathcal{X}}_t^{a,(p)} \\ \hat{\theta}_t^{a,(p)} \end{bmatrix} = \begin{bmatrix} \hat{P}_t^{xx} \\ \hat{P}_t^{\theta x} \end{bmatrix} H^\top \Gamma^{-1} \left(d\mathcal{Z}_t - \frac{1+\kappa}{2} H \hat{\mathcal{X}}_t^{a,(p)} dt - \kappa \Gamma^{1/2} d\hat{\mathcal{V}}_t^{(p)} - \frac{1-\kappa}{2} H \hat{m}_t^{xx} dt \right) \quad (10)$$

with $\hat{\mathcal{X}}_{t_0}^{a,(p)} = \hat{\mathcal{X}}_{t_1}^{f,(p)}$ and $\hat{\theta}_{t_0}^{a,(p)} = \hat{\theta}_{t_1}^{f,(p)} = \hat{\theta}_{t_0}^{f,(p)}$. This formulation highlights how the update in that substep does not alter the subspace spanned by the ensemble of particles, because of the left-multiplication of the rhs in eq. (10) by \hat{P}_t^{xx} , which keeps the dynamics of $\mathcal{X}_t^{a,(p)}$ in $\text{span}\{\hat{\mathcal{X}}_t^{f,(p)}, p = 1, \dots, P\}$. Rewriting the system in augmented state yields

$$d\hat{\mathcal{X}}_t^{a,(p)} = \hat{P}_t \bar{H}^\top \Gamma^{-1} \left(d\mathcal{Z}_t - \frac{1+\kappa}{2} \bar{H} \hat{\mathcal{X}}_t^{a,(p)} dt - \kappa \Gamma^{1/2} d\hat{\mathcal{V}}_t^{(p)} - \frac{1-\kappa}{2} \bar{H} \hat{m}_t dt \right).$$

Using a semi-implicit discretisation yields

$$\begin{aligned} (\mathbf{I}_{d+n_\theta} + \Delta t \hat{P}_{t_1}^f \bar{H}^\top \Gamma^{-1} \bar{H}) \hat{\mathcal{X}}_{t_1}^{a,(p)} \\ = \hat{\mathcal{X}}_{t_1}^{f,(p)} + \hat{P}_{t_1}^f \bar{H}^\top \Gamma^{-1} \left(\Delta \mathcal{Z}_{t_1} - \kappa \Gamma^{1/2} \Delta \hat{\mathcal{V}}_{t_1}^{(p)} - \frac{1-\kappa}{2} \bar{H} \left(\hat{m}_{t_1}^f - \hat{\mathcal{X}}_{t_1}^{f,(p)} \right) \Delta t \right), \end{aligned}$$

where $\hat{m}_{t_1}^f = \hat{m}(\hat{\mathcal{X}}_{t_1}^f)$ and $\hat{P}_{t_1}^f = \hat{P}(\hat{\mathcal{X}}_{t_1}^f)$. Assuming $\hat{P}_{t_1}^f$ invertible, we now left-multiply by $(\hat{P}_{t_1}^f)^{-1}$ and use the Woodbury identity to rewrite

$$\begin{aligned} \left[(\hat{P}_{t_1}^f)^{-1} (\mathbf{I}_{d+n_\theta} + \Delta t \hat{P}_{t_1}^f \bar{H}^\top \Gamma \bar{H}) \right]^{-1} &= \left[(\hat{P}_{t_1}^f)^{-1} + \bar{H}^\top (\Gamma / \Delta t)^{-1} \bar{H} \right]^{-1} \\ &= \hat{P}_{t_1}^f - \hat{P}_{t_1}^f \bar{H}^\top \left(\Gamma / \Delta t + \bar{H} \hat{P}_{t_1}^f \bar{H}^\top \right)^{-1} \bar{H} \hat{P}_{t_1}^f \\ &= (\mathbf{I}_{d+n_\theta} - \Delta t K_{t_1} \bar{H}) \hat{P}_{t_1}^f, \end{aligned}$$

where

$$K_{t_1} = \hat{P}_{t_1}^f \bar{H}^\top G_{t_1}^{-1} = \begin{bmatrix} \hat{P}_{t_1}^{xx,f} H^\top G_{t_1}^{-1} \\ \hat{P}_{t_1}^{\theta x,f} H^\top G_{t_1}^{-1} \end{bmatrix} = \begin{bmatrix} K_{t_1}^{xx} \\ K_{t_1}^{\theta x} \end{bmatrix}, \quad G_{t_1} = \Gamma + \Delta t \bar{H} \hat{P}_{t_1}^f \bar{H}^\top.$$

It is also possible to show by direct calculation that

$$(\mathbf{I}_{d+n_\theta} - \Delta t K_{t_1} \bar{H}) \hat{P}_{t_1}^f \bar{H}^\top \Gamma^{-1} = K_{t_1},$$

by which the analysis step can be rewritten as

$$\hat{\mathcal{X}}_{t_1}^{a,(p)} = (\mathbf{I}_{d+n_\theta} - \Delta t K_{t_1} \bar{H}) \hat{\mathcal{X}}_{t_1}^{f,(p)} + K_{t_1} \left(\Delta \mathcal{Z}_{t_1} - \kappa \Gamma^{1/2} \Delta \hat{\mathcal{V}}_{t_1}^{(p)} - \frac{1-\kappa}{2} \bar{H} \left(\hat{m}_{t_1}^f - \hat{\mathcal{X}}_{t_1}^{f,(p)} \right) \Delta t \right), \quad (11)$$

or equivalently, introducing $\eta = 1$,

$$\begin{bmatrix} \widehat{\mathcal{X}}_{t_1}^{a,(p)} \\ \widehat{\theta}_{t_1}^{a,(p)} \end{bmatrix} = \begin{bmatrix} \widehat{\mathcal{X}}_{t_1}^{f,(p)} \\ \widehat{\theta}_{t_1}^{f,(p)} \end{bmatrix} + \begin{bmatrix} K_{t_1}^{xx} \\ K_{t_1}^{\theta x} \end{bmatrix} \left(\Delta \mathcal{Z}_{t_1} - \frac{1+\kappa}{2} H \widehat{\mathcal{X}}_{t_1}^{f,(p)} \Delta t - \eta \kappa \Gamma^{1/2} \Delta \widehat{\mathcal{V}}_{t_1}^{(p)} - \eta \frac{1-\kappa}{2} H \widehat{m}_{t_1}^{x,f} \Delta t \right). \quad (12)$$

Following [21, Lemma 8.5], under the verifiable assumption of invertibility of Γ , it is possible to extend the analysis update formula to the case of singular \widehat{P}_t .

We will consider the following parameter combinations in our numerical experiments.

1. $\eta = 1, \kappa = 1$ (VENKF)
2. $\eta = 1, \kappa = 0$ (DENKF)
3. $\eta = 0, \kappa = 1$ (SENKF)

The VENKF discretisation corresponds to the usual forecast/analysis dynamics, and the same discretisation scheme is used to obtain the DENKF update. While the SENKF (“Sequential optimiser” ENKF) has a straightforward interpretation of computing the update using the observation-forecast mismatch of each particle, it is known [43] that it may underestimate analysis-error covariances, possibly causing filter divergence. On the other hand, this has an interpretation as a “sequential optimisation” which, for each particle, seeks the minimum of a weighted functional combining the deviation-from-observation mismatch and the deviation-from-forecast mismatch [33]. This procedure may be relevant in the case where the filtering distribution is not well-approximated by Gaussians.

Several Ensemble Square Root Kalman filters (including the Ensemble Adjustment Kalman Filter, the Ensemble Transform Kalman Filter, the unperturbed ENKF) are known to converge to the continuous time DENKF [20] in the limit of continuous observations (and suitably noise scalings). Adapting these filters to the low-rank context and studying their efficiency is of interest, but is beyond the scope of this work, and we shall not discuss this point further.

2.2.1 Connection to Discrete Observations

The setting devised in the above section assumes the observations to be given by a process, and is well-defined in the limit of $\Delta t \rightarrow 0$. In practice however, it can be of interest to recast the problem in a setting of discrete observations at each time step; this is in particular natural when the data stream consists in direct observations of the state rather than of stochastic increments. To that end, we detail how, for a fixed time-discretisation, the discretised analysis step can be understood as the discrete time Kalman-gain assimilation step, with a rescaled observation noise. For a fixed $\Delta t > 0$, define

$$y_{t_1} := \frac{\Delta \mathcal{Z}_{t_1}}{\Delta t} = H \mathcal{X}_{t_1}^{\text{true}} + \left(\frac{\Gamma}{\Delta t} \right)^{1/2} \xi_{t_1}, \quad \xi_{t_1} \sim \mathcal{N}(0, I_k).$$

Therefore, defining the rescaled observation noise level $\widetilde{\Gamma} = (\Gamma / \Delta t)$, eq. (12) is equivalent to

$$\begin{bmatrix} \widehat{\mathcal{X}}_{t_1}^{a,(p)} \\ \widehat{\theta}_{t_1}^{a,(p)} \end{bmatrix} = \begin{bmatrix} \widehat{\mathcal{X}}_{t_1}^{f,(p)} \\ \widehat{\theta}_{t_1}^{f,(p)} \end{bmatrix} + \begin{bmatrix} \widetilde{K}_{t_1}^{xx} \\ \widetilde{K}_{t_1}^{\theta x} \end{bmatrix} \left(y_{t_1} - \frac{1+\kappa}{2} H \widehat{\mathcal{X}}_{t_1}^{f,(p)} - \eta \kappa \widetilde{\Gamma}^{1/2} \widehat{\xi}_{t_1}^{(p)} - \eta \frac{1-\kappa}{2} H \widehat{m}_{t_1}^{x,f} \right). \quad (13)$$

with $\eta = 1$ and

$$\widetilde{K}_{t_1} = \widetilde{P}^f \widetilde{H}^\top \widetilde{G}_1^{-1} = \begin{bmatrix} \widetilde{P}_t^{xx,f} H^\top \widetilde{G}_{t_1}^{-1} \\ \widetilde{P}_t^{\theta x,f} H^\top \widetilde{G}_{t_1}^{-1} \end{bmatrix} = \begin{bmatrix} K_{t_1}^{xx} \\ K_{t_1}^{\theta x} \end{bmatrix}, \quad \widetilde{G}_{t_1} = \widetilde{\Gamma} + \widetilde{H} \widetilde{P}^f \widetilde{H}^\top.$$

Those correspond to the Ensemble Kalman update formulae in the discrete time setting.

We conclude this section by noting that the cost of simulating P augmented state particles scales like $\mathcal{O}(dP)$ (assuming the parameter dimension $n_\theta \ll d$). The computational cost may become prohibitively expensive when the state space dimension d is large, and offset only by choosing a small to moderate number of particles P . Unlike particle filters which often require a prohibitively large number of particles to prevent particle collapse, the Ensemble Kalman as introduced in [10] and its many variants are popular data assimilation tools in high dimensional problems, as empirically they perform satisfactorily well under a

small to moderate ensemble size. Note that both methods are still subject to catastrophic filter divergence and may require some stabilisation mechanism – that issue will not be addressed further in this work. Nevertheless, the possibility of increasing the number of particles remains of interest, as doing so can cause the ensemble to converge to a mean-field limit (if it exists) and hence subject to smaller sample variance. In the following section, we propose to perform a model order reduction by way of Dynamical Low-Rank approximations adapted to the Data Assimilation context, which will allow us to afford evolving larger ensembles thanks to the reduced computational cost of the model.

3 Dynamical Low-Rank State/Parameter estimation

This section firstly establishes the DLR-ENKF system used to efficiently propagate an ensemble of low-rank state particles alongside the ensemble of parameters. The small to moderate dimension of the parameter implies that no relevant gains should be expected when applying model order reduction techniques to the parameter ensemble; therefore, the DLR technique is only applied to the state particles. On the other hand we expect that the uncertainty on the parameters is reduced over time thanks to the continuous incoming stream of information. Hence, the state dynamics will also be less and less uncertain, justifying the use of dynamical low-rank methods. Additionally, we introduce a time-integration scheme that suitably combines a forecast/analysis-type discretisation with a robust time-integration scheme of the DLR system for the forecast step. A hyper-reduction technique is furthermore proposed to efficiently evaluate nonlinear terms in the (augmented state) dynamics.

In [29], the DLR methodology was used to perform a Dynamical Low-Rank approximation of the Kalman-Bucy Process (KBP), which corresponds to the dynamics (7) with an affine drift term f and possibly an extra additive noise term $\Sigma^{1/2}d\mathcal{W}_t$. The DLR method proposed in [29] approximates

$$\mathcal{X}_t^{\text{KBP}} \approx \mathcal{X}_t^{\text{DLR}} = U_t^0 + \sum_{i=1}^R U_t^i Y_t^i \equiv U_t^0 + \mathbf{U}_t \mathbf{Y}_t^\top,$$

by modifying the dynamics in such a way that it is possible to characterise the evolution of the factors in the right-hand-side. The above decomposition separates the process in its conditional mean $U_t^0 \in \mathbb{R}^d$ and a low-rank zero conditional mean part. Therefore, the stochastic modes $\mathbf{Y}_t \in [L^2(\Omega)]^R$ verify $\mathbb{E}[Y_t^i | \mathcal{A}_{\mathcal{Z}_t}] = 0$ in order to avoid redundancy with the mean. In this setting, the physical modes $\mathbf{U}_t \in \mathbb{R}^{d \times R}$ are orthogonal at all times, and consequently carry the information of the range of the covariance. The resulting process is named DLR-KBP.

The DLR-ENKF method also proposed in [29] is a particle approximation of DLR-KBP. It approximates the law of $\mathcal{X}_t^{\text{DLR}}$ by the ensemble $\hat{\mathcal{X}}_t^{\text{DLR}} = [\hat{\mathcal{X}}_t^{\text{DLR},(1)}, \dots, \hat{\mathcal{X}}_t^{\text{DLR},(P)}] \in \mathbb{R}^{d \times P}$ where

$$\hat{\mathcal{X}}_t^{\text{DLR},(p)} = \hat{U}_t^0 + \sum_{i=1}^R \hat{U}_t^i \hat{Y}_t^{i,(p)} \equiv \hat{U}_t^0 + \hat{\mathbf{U}}_t (\hat{\mathbf{Y}}_t^{(p)})^\top.$$

Notice that the deterministic modes $\{\hat{U}_t^i\}_{i=0}^R$ are common to all the particles, that is, all particles belong to the same affine low-dimensional space $\hat{U}_t^0 + \text{span}(\hat{U}_t^1, \dots, \hat{U}_t^R)$. We denote $\hat{\mathbf{Y}}_t^{(p)} = [\hat{Y}_t^{1,(p)}, \dots, \hat{Y}_t^{R,(p)}]$ the p -th R -dimensional particle in the reduced space $\text{span}(\hat{U}_t^1, \dots, \hat{U}_t^R)$ and $\hat{\mathbf{Y}}_t = [\hat{Y}_t^{(1)}; \dots; \hat{Y}_t^{(P)}] \in \mathbb{R}^{P \times R}$ the ensemble of reduced particles. In analogy to the mean-field case, $\hat{U}_t^0 = \mathbb{E}_P[\hat{\mathcal{X}}_t^{\text{DLR}}]$ is the sample conditional mean, $\hat{\mathbf{Y}}_t$ verify $\mathbb{E}_P[\hat{\mathbf{Y}}_t] = 0$, and the sample conditional covariance is given by $\hat{P}_t = \hat{\mathbf{U}}_t \hat{P}_{\hat{\mathbf{Y}}_t} \hat{\mathbf{U}}_t^\top$, where $\hat{P}_{\hat{\mathbf{Y}}_t} = \frac{1}{P-1} \hat{\mathbf{Y}}_t^\top \hat{\mathbf{Y}}_t$ is the reduced sample conditional covariance.

Extending the DLR-KBP and DLR-ENKF dynamics proposed in [29] to nonlinear dynamics involves a few caveats. The paper [29] actually proposes a DLR formulation for a general McKean-Vlasov SDE of the form

$$d\mathcal{X}_t = a(\mathcal{X}_t, t, \mu_t)dt + b(\mathcal{X}_t, t, \mu_t)d\mathcal{V}_t + c(\mathcal{X}_t, t, \mu_t)d\mathcal{Z}_t \quad (14)$$

with $\mu_t = \text{Law}(X_t)$, involving a Brownian motion \mathcal{V}_t and a general observation process \mathcal{Z}_t . Starting from this, it derives the DLR-KBP and DLR-ENKF processes for linear-affine dynamics. This latter assumption allows one to perform important simplifications. In this work we focus on nonlinear dynamics, therefore we start again from the DLR formulation for eq. (14) proposed in [29] and ‘‘formally’’ derive suitable DLR-KBP and DLR-ENKF processes for nonlinear dynamics. We focus first on the mean-field VENKF process (7) with $\kappa = 1$, which we rewrite here for convenience in the form of eq. (14), i.e.

$$\begin{aligned} d\mathcal{X}_t &= (f(\mathcal{X}_t, \theta_t) - P_t S \mathcal{X}_t) dt - P_t H^\top \Gamma^{-1/2} d\mathcal{V}_t + P_t H^\top \Gamma^{-1} d\mathcal{Z}_t \\ &= adt + bd\mathcal{V}_t + cd\mathcal{Z}_t, \end{aligned}$$

where $S = H^\top \Gamma^{-1} H$ and P_t is the (conditional) covariance of \mathcal{X}_t . Anticipating the developments below, the following quantities will be of interest.

$$\begin{aligned} \mathbb{E}[a | \mathcal{A}_{\mathcal{Z}_t}] &= \mathbb{E}[f(\mathcal{X}_t, \theta_t) | \mathcal{A}_{\mathcal{Z}_t}] - P_t S \mathbb{E}[\mathcal{X}_t | \mathcal{A}_{\mathcal{Z}_t}], & a_t^* &= f_t^*(\mathcal{X}_t, \theta_t) - P_t S \mathcal{X}_t^*, \\ \mathbb{E}[c | \mathcal{A}_{\mathcal{Z}_t}] &= P_t H^\top \Gamma^{-1}, & c_t^* &= 0, \end{aligned}$$

Using the above relations in the mean separated DO equations derived in [29, Section 3], we obtain the following system

$$\begin{aligned} dU_t^0 &= \mathbb{E}[f(\mathcal{X}_t, \theta_t) | \mathcal{A}_{\mathcal{Z}_t}] dt + P_t H^\top \Gamma^{-1} (d\mathcal{Z}_t - H U_t^0 dt), \\ d\mathcal{U}_t &= P_{\mathcal{U}_t}^\perp \mathbb{E}[f_t^*(\mathcal{X}_t, \theta_t) (\mathbf{Y}_t M_{\mathbf{Y}_t}^{-1}) | \mathcal{A}_{\mathcal{Z}_t}] dt, \\ d\mathbf{Y}_t^\top &= \mathcal{U}_t^\top f_t^*(\mathcal{X}_t, \theta_t) dt - \mathcal{U}_t^\top P_t H^\top \Gamma^{-1} (H \mathcal{X}_t^* + \Gamma^{1/2} d\mathcal{V}_t), \end{aligned}$$

where $M_{\mathbf{Y}_t} = \mathbb{E}[Y_t^i Y_t^j | \mathcal{A}_{\mathcal{Z}_t}]$ is the (continuous) Gram matrix. Based on these equations, and introducing a particle approximation, we obtain the DLR-VENKF system proposed in [29] for nonlinear dynamics

$$\begin{aligned} d\widehat{U}_t^0 &= \mathbb{E}_P[f(\widehat{\mathcal{X}}_t, \widehat{\theta}_t)] dt + \widehat{P}_t H^\top \Gamma^{-1} (d\mathcal{Z}_t - H \widehat{U}_t^0 dt - \Gamma^{1/2} d\mathbb{E}_P[\widehat{\mathcal{V}}_t]), \\ d\widehat{\mathcal{U}}_t &= P_{\widehat{\mathcal{U}}_t}^\perp \mathbb{E}_P[f_t^*(\widehat{\mathcal{X}}_t, \widehat{\theta}_t) \widehat{\mathbf{Y}}_t] \widehat{M}_{\widehat{\mathbf{Y}}_t}^{-1} dt, \\ d\widehat{\mathbf{Y}}_t^\top &= \widehat{\mathcal{U}}_t^\top f_t^*(\widehat{\mathcal{X}}_t, \widehat{\theta}_t) dt - \widehat{\mathcal{U}}_t^\top \widehat{P}_t H^\top \Gamma^{-1} (H \widehat{\mathcal{X}}_t^* + \Gamma^{1/2} d\widehat{\mathcal{V}}_t). \end{aligned} \tag{15}$$

where $\widehat{M}_{\widehat{\mathbf{Y}}_t} = \frac{1}{P} \widehat{\mathbf{Y}}_t^\top \widehat{\mathbf{Y}}_t$ denotes the empirical Gram matrix. Observe that the sample mean of the Brownian motions is subtracted from the equation for the stochastic modes to ensure that they remain (empirical) zero-mean, and is added back in the sample mean equation for consistency.

Performing the same steps for the DENKF process yields the following DLR-DENKF system

$$\begin{aligned} d\widehat{U}_t^0 &= \mathbb{E}_P[f(\widehat{\mathcal{X}}_t, \widehat{\theta}_t)] dt + \widehat{P}_t H^\top \Gamma^{-1} (d\mathcal{Z}_t - H U_t^0 dt), \\ d\widehat{\mathcal{U}}_t &= P_{\widehat{\mathcal{U}}_t}^\perp \mathbb{E}_P[f_t^*(\widehat{\mathcal{X}}_t, \widehat{\theta}_t) \widehat{\mathbf{Y}}_t] \widehat{M}_{\widehat{\mathbf{Y}}_t}^{-1} dt, \\ d\widehat{\mathbf{Y}}_t^\top &= \widehat{\mathcal{U}}_t^\top f_t^*(\widehat{\mathcal{X}}_t, \widehat{\theta}_t) dt - \frac{1}{2} \widehat{\mathcal{U}}_t^\top \widehat{P}_t H^\top \Gamma^{-1} H \widehat{\mathcal{X}}_t^* dt. \end{aligned} \tag{16}$$

3.1 Forecast-Analysis time-discretisation

The inverse Gram matrix $\widehat{M}_{\widehat{\mathbf{Y}}_t}^{-1}$ appearing in the above equations constitutes an additional source of stiffness when considering suitable time-integration of the above DLR systems. This consideration has led to the development of various robust time-integrators in the DLR literature, of which we mention the Basis Update and Galerkin (BUG) integrator [5, 28]. The time-integrator proposed in [29] has a BUG-like structure combined with Euler-Maruyama steps. In this work, we consider a different algorithm based on the forecast/analysis structure. The algorithm is again described over the time-interval $[t_0, t_1]$.

Forecast step. For both DLR-VENKF and DLR-DENKF, the dynamics is given by the first terms of eq. (15), dropping all the terms involving the Kalman gain

$$d\widehat{U}_t^0 = \mathbb{E}_P[f(\widehat{\mathcal{X}}_t, \widehat{\theta}_t)] dt, \quad d\widehat{\mathcal{U}}_t = P_{\widehat{\mathcal{U}}_t}^\perp \mathbb{E}_P[f_t^*(\widehat{\mathcal{X}}_t, \widehat{\theta}_t) \widehat{\mathbf{Y}}_t] \widehat{M}_{\widehat{\mathbf{Y}}_t}^{-1} dt, \quad d\widehat{\mathbf{Y}}_t^\top = \widehat{\mathcal{U}}_t^\top f_t^*(\widehat{\mathcal{X}}_t, \widehat{\theta}_t) dt.$$

Rather than updating the mean separately, we treat the solution $\widehat{U}_t^0 + \widehat{U}_t \widehat{\mathbf{Y}}_t^\top$ as a rank- $R+1$ function, which allows to straightforwardly use the BUG algorithm. The first step consists in computing augmented subspaces. To this end, denote $\widehat{\mathbf{Z}} = [\mathbf{1}, \widehat{\mathbf{Y}}_{t_0}]$ and $\widehat{\mathbf{V}} = [U_{t_0}^0, \mathbf{U}_{t_0}]$. Following [5] and adapting it to the present two-field decomposition, on $[t_0, t_1]$ we solve

$$\mathbf{K}(t_1) = \mathbf{K}(t_0) + \Delta t \mathbb{E}_P[f(\widehat{\mathbf{V}} \widehat{\mathbf{Z}}^\top, \widehat{\theta}_{t_0}) \widehat{\mathbf{Z}}], \quad \mathbf{L}(t_1)^\top = \mathbf{L}(t_0)^\top + \Delta t \widehat{\mathbf{V}}^\top f(\widehat{\mathbf{V}} \widehat{\mathbf{Z}}^\top, \widehat{\theta}_{t_0}),$$

and construct the augmented bases

$$\overline{\mathbf{U}} = \text{ortho}([\widehat{\mathbf{V}}, \mathbf{K}(t_1)]), \quad \overline{\mathbf{Y}} = \text{ortho}([\widehat{\mathbf{Z}}, \mathbf{L}(t_1)]).$$

The solution is then updated by Galerkin projection as follows

$$\mathbf{S}(t_1) = \mathbf{S}(t_0) + \Delta t \overline{\mathbf{U}}^\top \mathbb{E}_P[f(\widehat{\mathcal{X}}_{t_0}, \widehat{\theta}_t) \overline{\mathbf{Y}}],$$

The augmented solution is then $\widehat{\mathcal{X}}_{t_1}^{f,\text{aug}} = \overline{\mathbf{U}} \mathbf{S}(t_1) \overline{\mathbf{Y}}^\top$, which can also be written as $\widehat{\mathcal{X}}_{t_1}^{f,\text{aug}} = (\widehat{U}_{t_1}^0)^f + \overline{\mathbf{U}} \tilde{S}(t_1) \overline{\mathbf{Y}}^\top$ with $\mathbb{E}_P[\overline{\mathbf{U}} \tilde{S}(t_1) \overline{\mathbf{Y}}^\top] = 0$ since the constant vector $\mathbf{1}$ belongs to $\overline{\mathbf{Y}}$. Finally, truncate the zero-mean part to rank- R using a generalised SVD, yielding

$$\mathcal{T}_R \left(\overline{\mathbf{U}} \tilde{S}(t_1) \overline{\mathbf{Y}}^\top \right) = \widehat{\mathbf{U}}_{t_1}^f (\widehat{\mathbf{Y}}_{t_1})^\top. \quad (17)$$

The forecasted low-rank solution is given as $\widehat{\mathcal{X}}_{t_1}^f = (U_{t_1}^0)^f + \widehat{\mathbf{U}}_{t_1} (\widehat{\mathbf{Y}}_{t_1}^f)^\top$.

Analysis step. The analysis dynamics is

$$\begin{aligned} d\widehat{U}_t^0 &= \widehat{P}_t H^\top \Gamma^{-1} (d\mathcal{Z}_t - H \widehat{U}_t^0 dt - \kappa \Gamma^{1/2} d\mathbb{E}_P[\widehat{\mathcal{V}}_t]), \\ d\widehat{\mathbf{Y}}_t^\top &= \mathbf{U}_t^\top \widehat{P}_t H^\top \Gamma^{-1} \left(-\frac{1+\kappa}{2} H \widehat{\mathcal{X}}_t^\star dt - \kappa \Gamma^{1/2} d\widehat{\mathcal{V}}_t^\star \right), \end{aligned}$$

where we recall that \widehat{P}_t is the sample covariance. Note that we recover the DLR-VENKF scheme with $\kappa = 1$, and DLR-DENKF with $\kappa = 0$. The dynamics of the mean is structurally similar to the ENKF analysis dynamics as described in section 2.2, and consequently following the same steps as for the VENKF resp. DENKF to derive eq. (11) yields the update

$$(\widehat{U}_{t_1}^0)^a = (\widehat{U}_{t_1}^0)^f + K_{t_1} \left(\Delta \mathcal{Z}_{t_1} - H(\widehat{U}_{t_1}^0)^f \Delta t - \kappa \Gamma^{1/2} \mathbb{E}_P[\Delta \widehat{\mathcal{V}}_{t_1}] \right), \quad (18)$$

The Kalman gain K_{t_1} has a low-rank structure that will be detailed below. Conversely, the dynamics for $\widehat{\mathbf{Y}}_t$ can be interpreted as an update in the subspace $\text{span}(\widehat{\mathbf{U}}_{t_1})$. Indeed, recalling that $\widehat{P}_{t_1}^f = \widehat{\mathbf{U}}_{t_1} \widehat{P}_{\widehat{\mathbf{Y}}_{t_1}^f} \widehat{\mathbf{U}}_{t_1}^\top$, where $\widehat{P}_{\widehat{\mathbf{Y}}_{t_1}^f} = \frac{1}{P-1} (\widehat{\mathbf{Y}}_{t_1}^f)^\top \widehat{\mathbf{Y}}_{t_1}^f$, consider the semi-implicit discretisation

$$\begin{aligned} (\widehat{\mathbf{Y}}_{t_1}^a)^\top &= (\widehat{\mathbf{Y}}_{t_0}^a)^\top + \widehat{\mathbf{U}}_{t_1}^\top \widehat{P}_{t_1}^f H^\top \Gamma^{-1} \left(-H(\widehat{\mathcal{X}}_{t_1}^\star)^a \Delta t + \frac{1-\kappa}{2} H(\widehat{\mathcal{X}}_{t_1}^\star)^f \Delta t - \kappa \Gamma^{1/2} \Delta \widehat{\mathcal{V}}_{t_1}^\star \right) \\ &= (\widehat{\mathbf{Y}}_{t_0}^a)^\top + \widehat{P}_{\widehat{\mathbf{Y}}_{t_1}^f} H_U^\top \Gamma^{-1} \left(-H_U (\widehat{\mathbf{Y}}_{t_1}^a)^\top \Delta t + \frac{1-\kappa}{2} H_U (\widehat{\mathbf{Y}}_{t_1}^f)^\top - \kappa \Gamma^{1/2} \Delta \widehat{\mathcal{V}}_{t_1}^\star \right) \end{aligned}$$

where $H_U = H \mathbf{U}_{t_1}$. Therefore, following the same steps used to derive eq. (11) it holds

$$(\widehat{\mathbf{Y}}_{t_1}^a)^\top = (\widehat{\mathbf{Y}}_{t_1}^f)^\top + K_{t_1}^U \left(-\frac{1+\kappa}{2} H_U (\widehat{\mathbf{Y}}_{t_1}^f)^\top \Delta t - \kappa \Gamma^{1/2} \Delta \widehat{\mathcal{V}}_{t_1}^\star \right), \quad (19)$$

where

$$K_{t_1}^U = \widehat{P}_{\widehat{\mathbf{Y}}_{t_1}^f} H_U^\top (\Gamma + \Delta t H_U \widehat{P}_{\widehat{\mathbf{Y}}_{t_1}^f} H_U^\top)^{-1}.$$

Note that therefore,

$$\begin{aligned} \widehat{\mathbf{U}}_{t_1} (\widehat{\mathbf{Y}}_{t_1})^a &= \widehat{\mathbf{U}}_{t_1} (\widehat{\mathbf{Y}}_{t_1}^f)^\top + \widehat{\mathbf{U}}_{t_1} K_{t_1}^U \left(-\frac{1+\kappa}{2} H_U (\widehat{\mathbf{Y}}_{t_1}^f)^\top \Delta t - \kappa \Gamma^{1/2} \Delta \widehat{\mathcal{V}}_{t_1}^\star \right) \\ &= \widehat{\mathbf{U}}_{t_1} (\widehat{\mathbf{Y}}_{t_1}^f)^\top + K_{t_1} \left(-\frac{1+\kappa}{2} H \widehat{\mathbf{U}}_{t_1} (\widehat{\mathbf{Y}}_{t_1}^f)^\top \Delta t - \kappa \Gamma^{1/2} \Delta \widehat{\mathcal{V}}_{t_1}^\star \right) \end{aligned} \quad (20)$$

Combining eqs. (18) and (20), the analysis state $\widehat{\mathcal{X}}_{t_1}^a = (\widehat{U}_{t_1}^0)^a + \widehat{\mathbf{U}}_{t_1} (\widehat{\mathbf{Y}}_{t_1}^a)^\top$ verifies the same state update relation as eq. (12), which we rewrite here for clarity as

$$\widehat{\mathcal{X}}_{t_1}^a = \widehat{\mathcal{X}}_{t_1}^f + \widehat{\mathbf{U}}_{t_1} K_{t_1}^U \left(\Delta \mathcal{Z}_{t_1} - \frac{1+\kappa}{2} H \widehat{\mathcal{X}}_{t_1}^f \Delta t - \kappa \Gamma^{1/2} \Delta \widehat{\mathcal{V}}_{t_1} - \frac{1-\kappa}{2} \Delta t H \widehat{U}_{t_1}^0 \right). \quad (21)$$

Remark 3.1. In the forecast step, it is also possible to forego the explicit inclusion of the mean in the basis, keeping the remainder of the algorithm unchanged. While the mean is not explicitly tracked, it results in a more straightforward implementation, closer to the original BUG scheme [5].

Remark 3.2. In the truncation step (17), when the state has several variables, we truncate each variable separately rather than applying a single “global” truncation, since they may have different orders of magnitude. For example, in Section 4.2, the variables A and u appear in the augmented state as $(\hat{\mathcal{X}}_{t_1}^{f,\text{aug}})^\star = \begin{bmatrix} (\hat{\mathcal{X}}_{t_1}^{f,\text{aug}})_A^\star \\ (\hat{\mathcal{X}}_{t_1}^{f,\text{aug}})_u^\star \end{bmatrix}$, and the truncated state is obtained from the separate truncations $\mathcal{T}_R((\hat{\mathcal{X}}_{t_1}^{f,\text{aug}})_A^\star)$ and $\mathcal{T}_R((\hat{\mathcal{X}}_{t_1}^{f,\text{aug}})_u^\star)$. More precisely, assuming $2R \leq \min\{d, P\}$, we set

$$\hat{\mathbf{U}}_{t_1}^f = \begin{bmatrix} Q_A V_A & \\ & Q_u V_u \end{bmatrix} \quad \text{and} \quad \hat{\mathbf{Y}}_{t_1}^f = \bar{\mathbf{Y}} [W_A \Sigma_A \quad W_u \Sigma_u],$$

where $\bar{\mathbf{U}} = \begin{bmatrix} \bar{\mathbf{U}}_A \\ \bar{\mathbf{U}}_u \end{bmatrix}$, $\bar{\mathbf{U}}_A = Q_A R_A$ (resp. $\bar{\mathbf{U}}_u = Q_u R_u$) is the QR factorisation of $\bar{\mathbf{U}}_A$ (resp. $\bar{\mathbf{U}}_u$), and $R_A \tilde{S}(t_1) = V_A \Sigma_A W_A^\top$ (resp. $R_u \tilde{S}(t_1) = V_u \Sigma_u W_u^\top$) is the rank- R truncated SVD of $R_A \tilde{S}(t_1)$ (resp. $R_u \tilde{S}(t_1)$).

Remark 3.3. A rank-adaptive version of the scheme (like in [5]) is straightforwardly obtained by choosing a truncation threshold $\vartheta > 0$, and setting

$$R_{\text{new}} = \arg \min_{R \geq R_{\text{min}}} \left\{ R \mid \sum_{j=R+1}^{2R_{\text{old}}} \sigma_j^2(\tilde{S}(t_1)) \leq \vartheta^2, \right\} \quad (22)$$

in eq. (17) for some chosen $R_{\text{min}} \geq 1$, and where R_{old} is the current rank. The choice of the truncation parameter is critical, and must be fixed such that the algorithm captures the dominant dynamics while discarding the negligible ones. For an exceedingly small value, the rank may up to double at each iteration, rendering the algorithm impractical; conversely, for an exceedingly large threshold, the algorithm may discard significant dynamics, leading to accuracy loss.

Our proposed method has the potential to perform efficient data assimilation by dynamically evolving a low-rank analog of the ENKF. The accuracy of our method is contingent on the true filtering measure effectively exhibiting a nearly low-rank profile at all times, and in this context we discuss two linked but distinct potential effects that may degrade the signal-tracking ability of the DLR-ENKF. The first is the neglect of observation information, and the second is covariance under-approximation. Both of these effects stem from the low-rank approximation of the (range of the) covariance, which is the mechanism making our method efficient in the first place; after detailing the issues, we discuss possible mitigations.

The first effect expresses the fact that our method only assimilates the component of the (rescaled and state-space-embedded) observations $\tilde{\Delta \mathcal{Z}}_{t_1} = H^\top \Gamma^{-1} \Delta \mathcal{Z}_{t_1}$ lying in the range of $\hat{\mathbf{U}}_{t_1}$. This is readily seen from eq. (21); focussing on the Kalman gain part with the data increments,

$$\begin{aligned} K_{t_1}^U \Delta \mathcal{Z}_{t_1} &= \hat{P}_{\hat{\mathbf{Y}}_{t_1}^f} H_U^\top (\Gamma + \Delta t H_U \hat{P}_{\hat{\mathbf{Y}}_{t_1}^f} H_U^\top)^{-1} \Delta \mathcal{Z}_{t_1} \\ &= \hat{P}_{\hat{\mathbf{Y}}_{t_1}^f} \underbrace{\left[\mathbf{I}_R - H_U^\top \Gamma^{-1} H_U \left(\hat{P}_{\hat{\mathbf{Y}}_{t_1}^f}^{-1} / \Delta t + H_U^\top \Gamma^{-1} H_U \right)^{-1} \right]}_{=T} \hat{\mathbf{U}}_{t_1}^\top (H^\top \Gamma^{-1} \Delta \mathcal{Z}_{t_1}) \\ &= T \hat{\mathbf{U}}_{t_1}^\top \mathcal{P}_{\hat{\mathbf{U}}_{t_1}} \tilde{\Delta \mathcal{Z}}_{t_1}, \end{aligned}$$

having used the Woodbury identity in the second equality, and where $\mathcal{P}_{\hat{\mathbf{U}}_{t_1}} = \hat{\mathbf{U}}_{t_1} \hat{\mathbf{U}}_{t_1}^\top$. In particular, when $H = \mathbf{I}_d = \Gamma$, it holds

$$K_{t_1}^U \Delta \mathcal{Z}_{t_1} = T \hat{\mathbf{U}}_{t_1}^\top \mathcal{P}_{\hat{\mathbf{U}}_{t_1}} \Delta \mathcal{Z}_{t_1} = K_{t_1}^U \mathcal{P}_{\hat{\mathbf{U}}_{t_1}} \Delta \mathcal{Z}_{t_1},$$

and hence the DLR-ENKF only assimilates the component of the observations in the subspace of $\widehat{\mathbf{U}}_{t_1}$. Note that the ENKF operates under the same principle, assimilating the observations only in the subspace spanned by the particles. The distinction is that, in the common regime $P \ll d$, this subspace is (at most) P -dimensional rather than being limited at R . However, when the P particles concentrate on an R -dimensional subspace that the DLR-ENKF identifies, the assimilations performed by the ENKF and the DLR-ENKF are expected to be comparable.

The second effect is related to the potential under-approximation of the sample covariance due to rank underestimation. Consider the setting where the full order model ENKF has a covariance $\widehat{P}_t^{\text{ENKF}}$ with a suitable low-rank approximation of rank R' . If the system is simulated using the DLR-ENKF method using a rank $R < R'$, and for simplicity assuming that $\widehat{P}_t^{\text{DLR}} \approx \mathcal{T}_R(\widehat{P}_t^{\text{ENKF}})$, it holds

$$\|\widehat{P}_t^{\text{DLR}}\|_F^2 \approx \|\mathcal{T}_R(\widehat{P}_t^{\text{ENKF}})\|_F^2 = \sum_{i=1}^R \lambda_i^2(\widehat{P}_t^{\text{ENKF}}) < \sum_{i=1}^{R'} \lambda_i^2(\widehat{P}_t^{\text{ENKF}}) \approx \|\widehat{P}_t^{\text{ENKF}}\|_F^2.$$

In effect, the DLR-ENKF may underestimate the true covariance of the system, causing it to express higher confidence in a given state than warranted; furthermore, increasing the rank may at first cause the uncertainty to *increase* before stabilising when the rank is sufficiently large. In our numerical results, the issue of uncertainty under-approximation seems to be more prevalent than the issue of neglecting the signal. This can however be corrected by choosing a sufficiently large rank *a priori*. Another approach could integrate a rank-adaptive strategy to control the covariance under-approximation and observations neglect, in the spirit of [12]. Those considerations are however outside of the scope of this work, and will not be discussed further here.

3.2 Hyper-reduction

When $f_t^*(\widehat{\mathcal{X}}_t, \widehat{\theta}_t)$ is nonlinear with respect to $\widehat{\mathcal{X}}_t$, the evaluation of $\mathbb{E}_P[f_t^*(\widehat{\mathcal{X}}_t, \widehat{\theta}_t)\widehat{\mathbf{Y}}_t]$ and $\mathbf{U}_t^\top f_t^*(\widehat{\mathcal{X}}_t, \widehat{\theta}_t)$ scales with $d \times P$ (instead of $d \times R$ and $R \times P$). To reduce this cost, we employ a CUR approximation based on the discrete empirical interpolation method (DEIM) [2, 7]. The idea is to approximate the nonlinear term $f_t^*(\widehat{\mathcal{X}}_t, \widehat{\theta}_t) \in \text{Mat}(d \times P)$ by evaluating it only at a few row $\{\sigma_t^1, \dots, \sigma_t^n\}$ and column $\{\varsigma_t^1, \dots, \varsigma_t^m\}$, with $n \ll d$ and $m \ll P$. Let $\mathbf{P}_\sigma \in \text{Mat}(n \times d)$ (resp. $\mathbf{P}_\varsigma^\top \in \text{Mat}(P \times m)$) denote the matrix extracting the rows indexed by $\sigma = \{\sigma_t^1, \dots, \sigma_t^n\}$ (resp. columns indexed by $\varsigma = \{\varsigma_t^1, \dots, \varsigma_t^m\}$). The nonlinear term is approximated by the CUR factorisation

$$f_t^*(\widehat{\mathcal{X}}_t, \widehat{\theta}_t) \approx \left(f_t^*(\widehat{\mathcal{X}}_t, \widehat{\theta}_t) \mathbf{P}_\varsigma^\top \right) \left(\mathbf{P}_\sigma f_t^*(\widehat{\mathcal{X}}_t, \widehat{\theta}_t) \mathbf{P}_\varsigma^\top \right)^+ \left(\mathbf{P}_\sigma f_t^*(\widehat{\mathcal{X}}_t, \widehat{\theta}_t) \right)^\top, \quad (23)$$

where $(\cdot)^+$ stands for the Moore–Penrose pseudoinverse. The indices $\{\sigma_t^1, \dots, \sigma_t^n\}$ and $\{\varsigma_t^1, \dots, \varsigma_t^m\}$ are selected by the DEIM, with $n = R$ and $m = 2R$. Specifically, R columns $\varsigma = \{\varsigma_t^1, \dots, \varsigma_t^R\}$ are first chosen by Algorithm 1 with input $\text{ortho}(\widehat{\mathbf{Y}}_t)$. This corresponds to choosing R particles. Then, R rows $\sigma = \{\sigma_t^1, \dots, \sigma_t^R\}$ are selected using Algorithm 1 with input $\text{ortho}(f_t^*(\widehat{\mathcal{X}}_t, \widehat{\theta}_t) \mathbf{P}_\varsigma^\top)$, where $\mathbf{P}_\varsigma^\top \in \text{Mat}(P \times R)$ extracts the columns indexed by ς . Finally, R additional columns $\{\varsigma_t^{R+1}, \dots, \varsigma_t^{2R}\}$ are chosen using Algorithm 1 with input $\text{ortho}(\mathbf{P}_\sigma f_t^*(\widehat{\mathcal{X}}_t, \widehat{\theta}_t))$. Thus, the final $\mathbf{P}_\varsigma^\top$ in (23) extracts the $2R$ columns indexed by $\varsigma = \{\varsigma_t^1, \dots, \varsigma_t^{2R}\}$. Compared to the approach described in [9], this CUR approximation presents two main differences: (1) the sampling indices $\{\sigma_t^1, \dots, \sigma_t^R\}$ are determined from the left basis of the nonlinear term $f_t^*(\widehat{\mathcal{X}}_t, \widehat{\theta}_t) \mathbf{P}_\varsigma^\top$ (which is more appropriate than using the left basis of the solution at the previous time-step), and (2) an oversampling of R additional columns is used to improve accuracy.

Algorithm 1 DEIM point selection algorithm [7]

Input: An orthonormal matrix $\mathbf{Q} \in \mathbb{R}^{n \times m}$
Output: A vector $\mathbf{p} \in \mathbb{R}^m$ containing the indices $\{\sigma^1, \dots, \sigma^m\}$

- 1: $\mathbf{q} = \mathbf{Q}(:, 1)$
- 2: $[\sim, \sigma^1] = \max(|\mathbf{q}|)$
- 3: $\mathbf{p} = [\sigma^1]$
- 4: **for** $j = 2, \dots, m$ **do**
- 5: $\mathbf{q} = \mathbf{Q}(:, j)$
- 6: $\mathbf{r} = \mathbf{q} - \mathbf{Q}(:, 1:j-1) (\mathbf{Q}(\mathbf{p}, 1:j-1))^{-1} \mathbf{q}(\mathbf{p})$
- 7: $[\sim, \sigma^j] = \max(|\mathbf{r}|)$
- 8: $\mathbf{p} = [\mathbf{p}; \sigma^j]$
- 9: **end**

4 Numerical experiments

This section assesses the qualities of the proposed DLR-ENKF method for parameter identification by benchmarking it on two examples, a Fisher-KPP problem and a reduced one-dimensional blood flow model of the 55 arteries in the human body. These two models already showcase several relevant properties of the method, which are discussed in detail in the sections. To summarise our findings, for a moderate rank R the DLR-ENKF consistently performs the same level of data assimilation and parameter identification as its ENKF counterpart, and consistently does so at a reduced computational cost. The DEIM hyper-reduction proves effective in reducing the cost for hyper-quadratic nonlinearities (but offers no substantial gains for quadratic nonlinearities). One key finding of our numerical experiments is that the accuracy of DLR-ENKF is highly dependent on the approximation rank R , which must be chosen large enough to capture the rank of the state ensemble *a priori*. If the rank is too small, the DLR-ENKF may under-estimate the covariance, eventually leading to inaccurate assimilation and parameter identification. This naturally calls for rank-adaptive strategies, which will be explored in this work and investigated further in future works.

4.1 Fisher–Kolmogorov–Petrovski–Piskunov system

The following experimental setting is inspired by the one in [31]. The dynamics is given by (the discretisation of) a Fisher–Kolmogorov–Petrovski–Piskunov (Fisher-KPP) reaction-diffusion equation, which models the evolution of biological population invasions, genes, or chemical reactions over space and time. On the domain

$$D = \left\{ (x, y) \in \mathbb{R}^2 \mid 1 \leq \sqrt{x_1^2 + x_2^2} \leq 1.5, x_1 \geq 0, x_2 \geq 0 \right\},$$

denote $u(t, x, \theta)$ the solution on $(0, T)$ with $T = 0.154$ to

$$\begin{aligned} \partial_t u(t, x, \theta) - \operatorname{div}(\nu(x, \theta) \nabla u) - 75u(1-u) &= 0, & x \in D, t \in (0, T) \\ \nu(x, \theta) \nabla u(t, x, \theta) \cdot \mathbf{n} &= 0, & x \in D, t \in (0, T) \\ u(0, x, \theta) &= \exp(-(x_1 - 1.5)^2 - 50x_2^2) & x \in D. \end{aligned}$$

In this problem setting, the concentration u diffuses with a preferential direction along the tangential direction of the annulus arc with a wave-front structure; by $T = 0.154$, the wave-front has traversed almost the whole domain. The physical discretisation is performed via the Finite Element Method, using $\mathbb{P}_1^C(\mathcal{T}_h)$ the space of \mathbb{P}_1 -continuous finite elements on the quasi-uniform mesh $\mathcal{T}_h \subset D$. Furthermore, denote $d = \dim(\mathbb{P}_1^C(\mathcal{T}_h)) = 540$. The time-step discretisation is set to $\Delta t = 4.4 \cdot 10^{-5}$, and we use the explicit Euler method for the forecast step in the ENKF, and the explicit BUG method for the forecast in the DLR-ENKF detailed in section 3.1.

For the diffusion coefficient, we follow [31] and define the parametric diffusion coefficient at the discrete level by the Karhunen-Loëve-like expansion

$$\nu(x, \theta) = \sqrt{2} + \sum_{i=1}^{n_\theta} \theta_i \sqrt{\lambda_i} \xi_i(x),$$

where ξ_i , $i = 1, \dots, n_\theta$ are the first n_θ ordered eigenfunctions of

$$C_{ij} = a \exp\left(-\frac{\|x^i - x^j\|}{2b^2}\right) + c\delta_{ij}, \quad 1 \leq i, j \leq d,$$

where δ_{ij} is a Kronecker symbol, $a = 1$, $b = 1$, $c = 0.1$ and $\{x^i\}_{i=1}^d \subset \mathcal{T}_h$ are the mesh nodes. The eigenfunctions ξ_i are depicted in Figure 1. In order to ensure $\nu(x, \theta) > 0$, the parameters are constrained to the hypercube

$$\mathcal{Q}_{n_\theta} = \left\{ \theta \in \mathbb{R}^{n_\theta} \mid \max_{i=1, \dots, n_\theta} |\theta_i| \leq \sqrt{2} \left(\sum_{i=1}^{n_\theta} \sup_{x \in D} \sqrt{\lambda_i} |\xi_i(x)| \right)^{-1} \right\}.$$

In this example, we consider $n_\theta = 6$, and set

$$\theta^{\text{true}} = (0.271, 0.266, 0.504, -0.111, -0.014, -0.086)^\top \in \mathcal{Q}_{n_\theta}. \quad (24)$$

Then, we sample a perturbed $\theta^{\text{perturbed}} \sim \mathcal{N}(\theta^{\text{true}}, 0.05^2 \mathbf{I}_{n_\theta})$ and set the initial conditions of the ensemble as $\hat{\theta}_0^{(i)} \sim \mathcal{N}(\theta^{\text{perturbed}}, 0.05^2 \mathbf{I}_{n_\theta})$ for $i = 1, \dots, P = 200$. The ensemble of state particles is initialised with the same initial condition $\mathcal{X}_0^{(i)} = I_h(\exp(-(x_1 - 1.5)^2 - 50x_2^2))$ for all the particles $i = 1, \dots, P$, where I_h is the FE interpolation operator.

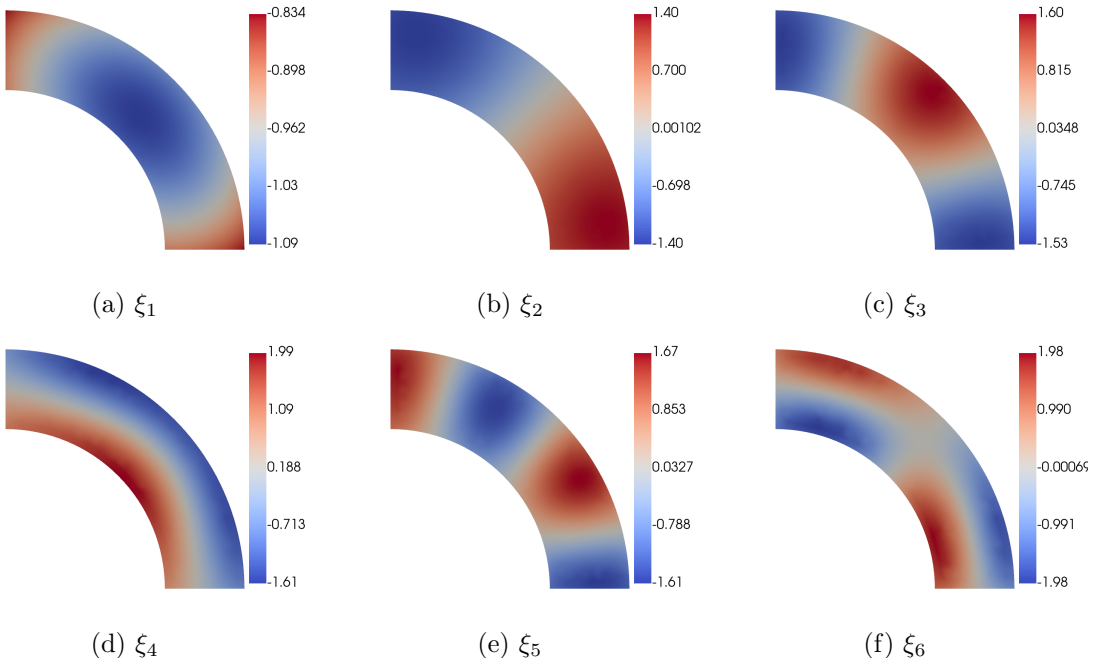


Figure 1: Modes of the diffusion coefficient $\nu(x)$

We consider two observation scenarios, full ($h^{\text{full}} = id$) and partial observations. The partial observation operator h^{part} is defined as

$$(h^{\text{part}} u(x))_i = \frac{30}{0.05\pi} \int_D \exp\left(-\frac{(x - x_i)^2 + (y - y_i)^2}{2(0.05)^2}\right) u(x) dx dy,$$

for $(x_i, y_i) = (\rho \cos \alpha, \rho \sin \alpha)$ and where $\rho \in \{1, 1.5\}$ and $\alpha \in \{\pi/2, \pi/3, \pi/4, \pi/6\}$ for all possible combinations. Consequently, $h^{\text{part}} u \in \mathbb{R}^8$. The true signal is generated using an

explicit Euler scheme with the time-discretisation $\Delta t = 4.4 \cdot 10^{-5}$, the observations are computed for that time-discretisation. Additionally, in either cases of full ($k = d$) or partial ($k = 8$) observations, we set $\Gamma = \gamma \mathbf{I}_k$ with $\gamma = 10^{-8}$.

As the nonlinearities in the augmented state are quadratic in this example and the ranks considered are sufficiently small, we do not apply the DEIM here (the speed-ups obtained by applying it are minor for the present problem settings).

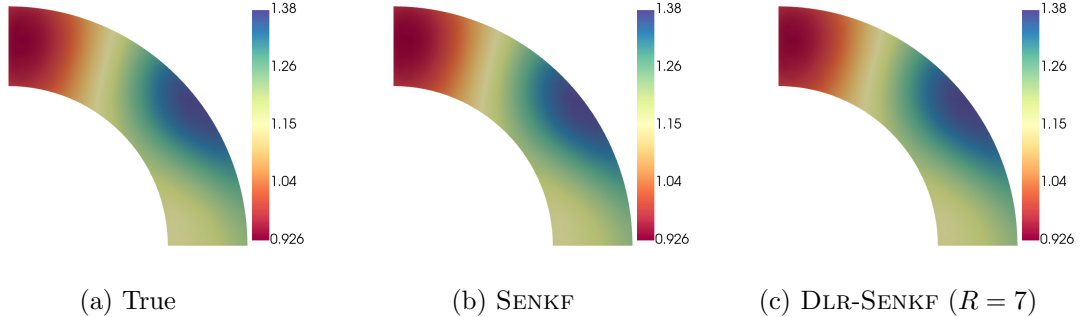


Figure 2: True and identified diffusion coefficient $\nu(x, \theta)$ at final time (full observations)

For both observation scenarios, we compare the VENKF, DENKF and SENKF to their DLR counterparts for varying ranks $R = 2, 5, 7$. For the DLR-ENKF schemes, we used the explicit BUG scheme combined with the analysis step as outlined in section 3.1. To keep the comparisons fair, all of the other parameters are identical to the ENKF case, in particular using $P = 200$ particles and $\Delta t = 4.4 \cdot 10^{-5}$. In Figure 2 we compare the true field $\nu(x)$ to the one obtained by the SENKF algorithm, as well as the DLR-SENKF. Their similarity is further verified when examining the evolution of the ensemble of parameters. Figure 3 displays the parameter identification achieved by the SENKF. The filter correctly identifies all the parameters (with minor biases for $\theta_2, \theta_4, \theta_6$). Similarly, Figure 4 displays the same quantities when using the DLR-SENKF filter with rank 7. Observe that the plots are very similar, suggesting that this rank is already enough to suitably capture the filtering density as it evolves in time.

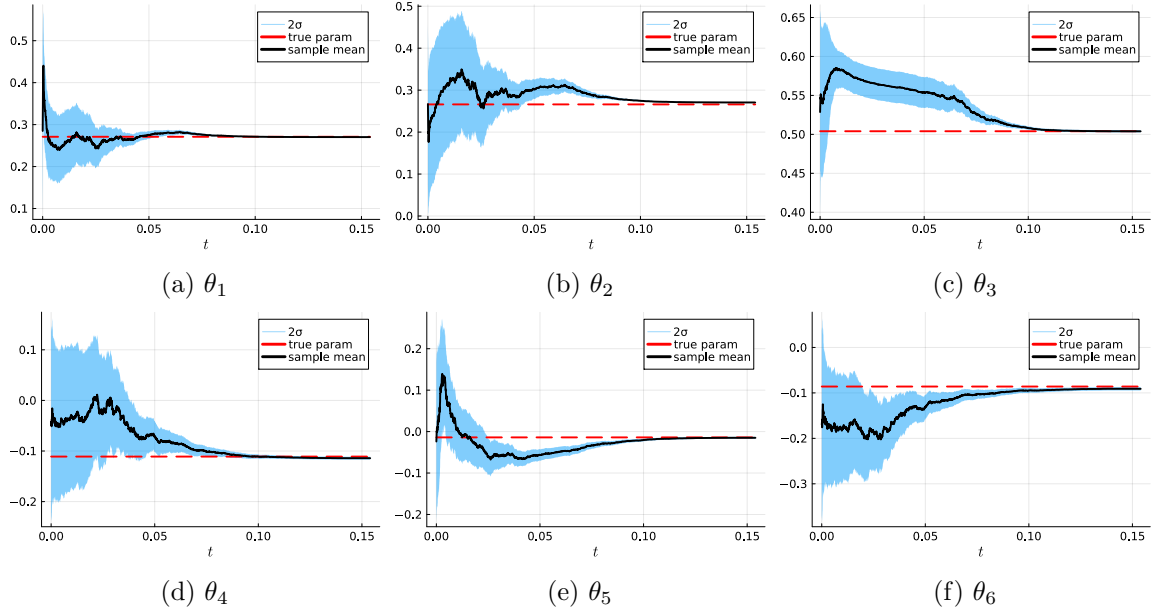


Figure 3: Full Order Model SENKF parameter identification with $P = 200$ particles (full observations)

The relative errors $\|\mathbb{E}_P[\hat{\theta}_T] - \theta^{\text{true}}\| / \|\theta^{\text{true}}\|$ are displayed in Table 1 for all combinations of methods (SENKF, VENKF, DENKF) and both observation scenarios (averaged over 10 runs).

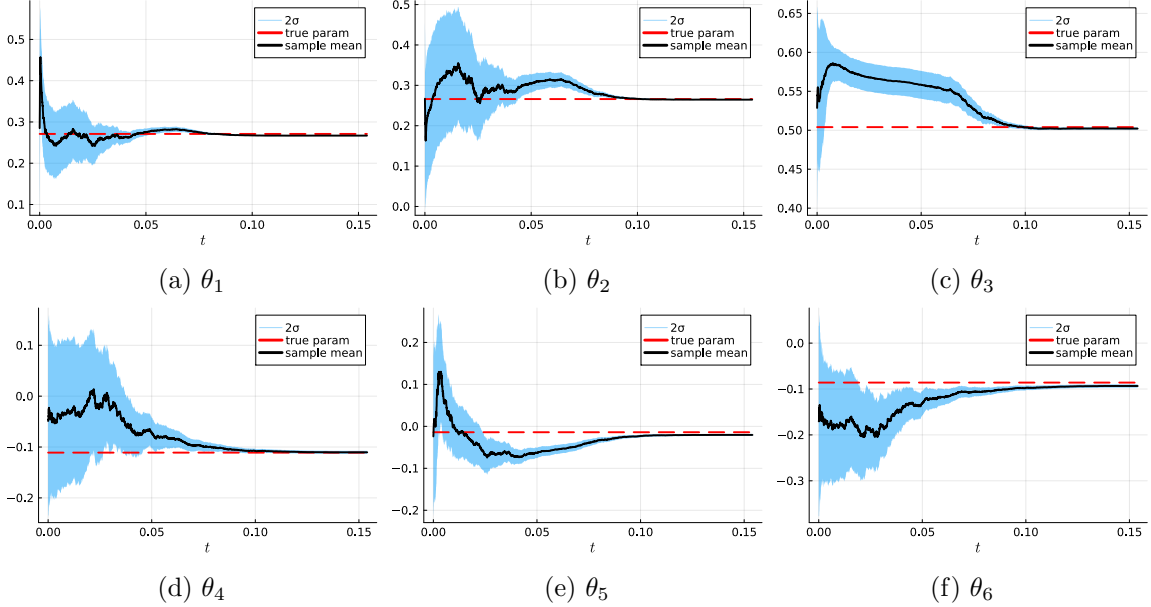


Figure 4: DLR-SENKF ($R = 7$) parameter identification with $P = 200$ particles (full observations)

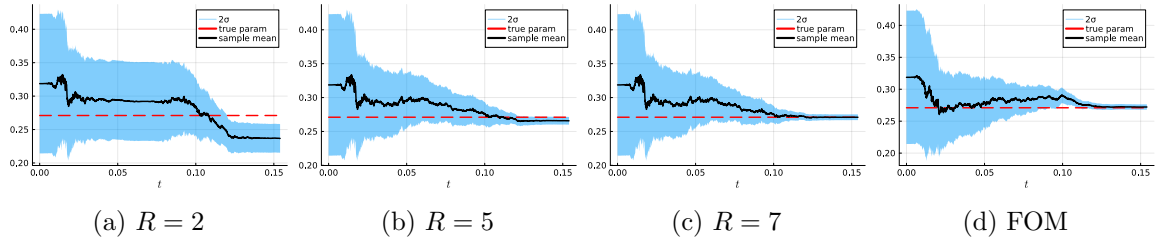


Figure 5: Parameter θ_1 for partial observations ($P = 200$); (a)–(c) DLR-SENKF (d) SENKF

Throughout the methods, it is seen that increasing the rank correlates with a decreasing relative error. In the case of full observation, the relative error approaches that obtained by the full order model. It is noteworthy that in the case of partial observations, the ENKF is (at least initially) not well-approximated by a subspace of rank 7 or less. This is indirectly seen in figs. 5 and 6, as the evolution of the ensemble of parameter of θ_1 and θ_2 for the DLR-SENKF are distinct from the SENKF. Despite developing a distinct solution, the DLR-ENKF correctly identifies θ_1 , but fails for θ_2 . This showcases two effects: (a) the DLR-ENKF distinct from the true solution *can* still perform an adequate signal-tracking and parameter identification (notably, it was observed several times in simulations that the relative errors of the DLR-ENKF filters were eventually *lower* than their ENKF counterparts – not shown in figures); (b) however, augmenting the rank is sometimes necessary to ensure consistency with the underlying ENKF (and in this case, ensure successful parameter identification).

Additionally, the timings are displayed in Table 2. Thanks to the low-rank structure, the DLR-ENKF versions are always faster than their full order ENKF counterparts, and, predictably, the computational cost increases with the rank. It is expected that speed-ups can be even more important in the case of stronger nonlinearities, much finer FE discretisations, and combinations with the DEIM technique.

Finally, we explore the integration of rank-adaptivity in the assimilation scheme. Rank-adaptive methods are of particular interest in the filtering context, as it is common for the filtering distribution to eventually concentrate on a low-dimensional subspace (or even collapse onto a single point); using an increasingly smaller rank may prove to be sufficient to accurately evolve the filtering distribution. This experiment considers the case of full observations, and the truncation threshold is fixed to $\vartheta = 2 \cdot 10^{-8}$. As the initial condi-

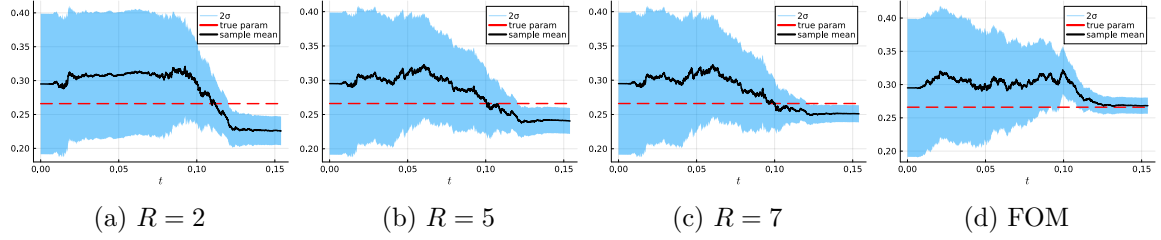


Figure 6: Parameter θ_2 for partial observations ($P = 200$); (a)–(c) DLR-SENKF (d) SENKF

	DLR			FOM
	$R = 2$	$R = 5$	$R = 7$	
SENKF	0.585	0.013	0.014	0.012
VENKF	0.660	0.018	0.011	0.008
DENKF	0.275	0.014	0.008	0.006

(a) Full observations

	DLR			FOM
	$R = 2$	$R = 5$	$R = 7$	
SENKF	0.191	0.096	0.092	0.077
VENKF	0.240	0.112	0.109	0.088
DENKF	0.232	0.113	0.111	0.086

(b) Partial observations

Table 1: Relative errors $\|\mathbb{E}_P[\hat{\theta}_T] - \theta^{\text{true}}\| / \|\theta^{\text{true}}\|$ (averaged over 10 runs)

	DLR			FOM
	$R = 2$	$R = 5$	$R = 7$	
SENKF	4.7	9.2	14.4	18.2
VENKF	4.7	9.3	13.8	18.6
DENKF	4.4	8.6	13.9	17.6

(a) Full observations

	DLR			FOM
	$R = 2$	$R = 5$	$R = 7$	
SENKF	5.7	11.2	15.0	19.3
VENKF	4.3	9.1	14.4	18.4
DENKF	4.2	9.0	13.9	18.0

(b) Partial observations

Table 2: Timings [mins]

	SENKF	VENKF	DENKF		SENKF	VENKF	DENKF
adaptive	0.030	0.011	0.007		16.3	15.4	14.1
fixed	0.007	0.012	0.005		20.2	18.6	17.8
(a) $\ \mathbb{E}_P[\hat{\theta}_T] - \theta^{\text{true}}\ /\ \theta^{\text{true}}\ $				(b) Timings [min]			

Table 3: Fixed/adaptive ranks (single run, full observations, truncation threshold $\vartheta = 2 \cdot 10^{-8}$).
(a) Relative errors (b) Timings

tion has rank 1, the solution is evolved using the fixed-rank algorithm over the first 200 iterations (with $R_{\text{initial}} = 7$). This warm start procedure allows the numerical solution to suitably develop its features before activating the rank-adaptive mechanism. Additionally, we fix $R_{\min} = 2$ in eq. (22), which ensures that the covariance is not degenerate. The rank evolutions are displayed in Figure 7. The expected rank decrease consistent with filtering density collapse is observed across all methods. Furthermore, DLR-VENKF and DLR-DENKF roughly truncate at the same moments in time, whereas DLR-SENKF tends to truncate earlier. Precocious truncation can negatively impact the solution accuracy, which is (indirectly) corroborated by Table 3a. Indeed, while the rank-adaptive DLR-VENKF and DLR-DENKF schemes identify the parameter at the same level of accuracy as their fixed-rank counterparts, the rank-adaptive DLR-SENKF performs significantly worse than its fixed-rank counterpart. The timings are displayed in Table 3b and show a modest speed-up, which is not surprising given the relatively small initial rank. Significantly higher speed-ups are expected for problems with higher initial ranks and finer discretisations.

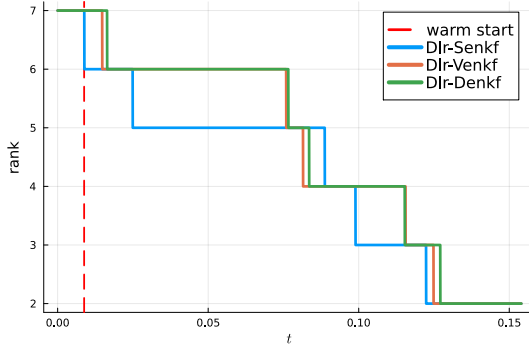


Figure 7: Ranks for rank-adaptive schemes (full observations, $\vartheta = 2 \cdot 10^{-8}$).
Rank-adaptivity starts at warm start.

4.2 One-dimensional reduced blood flow model

The second numerical experiment, inspired by [24], aims to estimate the aortic stiffness of a one-dimensional reduced blood flow model using peripheral measurements. This model represents the blood flow in the 55 main human arteries (see Figure 8). It is derived from the three-dimensional incompressible Navier–Stokes equations by assuming that (1) vessel curvature is negligible, (2) vessels are axisymmetric, and (3) vessel properties are constant (see [11] for details). Under these assumptions, the mass and momentum equations reduce to

$$\frac{\partial \mathbf{U}}{\partial t} + \frac{\partial \mathbf{F}(\mathbf{U})}{\partial x} = \mathbf{S}(\mathbf{U}), \quad (25)$$

where

$$\mathbf{U} = \begin{bmatrix} A \\ u \end{bmatrix}, \quad \mathbf{F} = \begin{bmatrix} Q \\ \frac{u^2}{2} + \frac{p}{\rho} \end{bmatrix}, \quad \mathbf{S} = \begin{bmatrix} 0 \\ -\nu \frac{u}{A} \end{bmatrix},$$

with x the axial coordinate along the vessel, A the cross-sectional area, u the mean fluid velocity, $Q = Au$ the flow rate, p the fluid pressure, $\rho = 1050 \text{ kg m}^{-3}$ the fluid density, and

$\nu = 9 \times 10^{-6} \text{ m}^2 \text{ s}^{-1}$ the viscous resistance. This system (25) is closed by assuming that the vessel wall follows an elastic law, leading to the pressure-area relation:

$$p = p_{\text{ext}} + \beta(\sqrt{A} - \sqrt{A_0}), \quad (26)$$

where $p_{\text{ext}} = 11\,465.692 \text{ Pa}$ is the external pressure, β is the elastic coefficient, and A_0 is the cross-sectional area at rest. The conservative system (25) is hyperbolic because the Jacobian matrix

$$\frac{\partial \mathbf{F}}{\partial \mathbf{U}} = \begin{bmatrix} u & A \\ \frac{\beta}{2\sqrt{A}} & u \end{bmatrix}$$

has two real eigenvalues $\lambda_{1,2} = u \pm c$, and the characteristic variables are $W_{1,2} = u \pm 4c$, with $c = \sqrt{\frac{\beta}{2\rho}} A^{1/4}$ the wave speed propagation. In physiological conditions, the flow is subsonic with $c \gg u$. System (25) is completed with suitable boundary conditions. At the inlet of the ascending aorta, we prescribe a periodic inflow of the form

$$A(t) = a_0 + \sum_{k=1}^4 (a_k \cos(k\omega t) + b_k \sin(k\omega t)), \quad (27)$$

where $a_0 = 7.441 \times 10^{-4}$, $a_1 = -2.809 \times 10^{-5}$, $b_1 = 4.699 \times 10^{-5}$, $a_2 = -3.094 \times 10^{-5}$, $b_2 = 3.497 \times 10^{-6}$, $a_3 = -5.753 \times 10^{-6}$, $b_3 = -1.405 \times 10^{-5}$, $a_4 = 1.557 \times 10^{-6}$, $b_4 = -2.932 \times 10^{-6}$, and $\omega = 2\pi/T$ with $T = 0.8 \text{ s}$ the period of a cardiac cycle. At the terminal nodes, non-reflecting boundary conditions are imposed:

$$\frac{dW_2}{dt} = -\nu \frac{u}{A}. \quad (28)$$

At the bifurcation nodes, the conservation of mass flux and the continuity of total pressure reduce to the conditions

$$\begin{aligned} Q_{\text{in}} &= Q_{\text{out}_1} + Q_{\text{out}_2}, \\ \left(\rho \frac{u^2}{2} + p \right)_{\text{in}} &= \left(\rho \frac{u^2}{2} + p \right)_{\text{out}_1} = \left(\rho \frac{u^2}{2} + p \right)_{\text{out}_2}. \end{aligned} \quad (29)$$

To ensure that the number of equations matches the number of unknowns at vessel boundaries and bifurcations, systems (27)–(29) are completed with the standard compatibility relations (see [11] for details). These relations enforce the correct coupling of characteristic variables and lead to the solution of local nonlinear systems of size 2×2 (at vessel boundaries) and 6×6 (at bifurcations). Physiological properties of the arterial tree are taken from [23] and summarised in Table 6. The resulting blood flow model is integrated in time using the forward Euler method and fixed time-step size $\Delta t = 5 \times 10^{-5}$. In space, a second-order finite volume method based on the MUSCL reconstruction [42] and local Lax-Friedrichs numerical flux [22] is used with the uniform mesh size $\Delta x = 2 \times 10^{-3}$, leading to $d = 3542$ DOFs.

The objective is now to estimate the elastic coefficient of the ascending aorta (n°1) and aortic arch I (n°13), i.e. $\theta^{\text{true}} = [\beta_1 \ \beta_{13}]$, while assuming all other parameters are known. For this purpose, we collect measurements of fluid velocity and cross-sectional area at the midpoint of three arteries—the left external carotid (n°15), left radial (n°21), and right femoral (n°46)—yielding $k = 6$ observations at each time-step. The observation noise covariance is

$$\Gamma = \begin{bmatrix} \sigma_A \mathbf{I}_3 & \\ & \sigma_u \mathbf{I}_3 \end{bmatrix},$$

where $\sigma_A = 10^{-2}$ and $\sigma_u = 10^{-7}$, corresponding to about 5% noise. The ensemble is initialised with $P = 100$ particles sampled as $\hat{\theta}_0^{(i)} \sim \mathcal{N}(\theta^{\text{perturbed}}, \sigma_\theta^2 \mathbf{I}_2)$, where $\theta^{\text{perturbed}} \sim \mathcal{N}(\theta^{\text{true}}, \sigma_\theta^2 \mathbf{I}_2)$ and $\sigma_\theta = 10^5$. In order to initialise the state associated to each particle, we start from the system at rest (i.e., $A = A_0$ and $u = 0$), and we perform two cardiac cycles (corresponding to 1.6 s or 32 000 time-steps) to reach a quasi-periodic flow. Then, we collect observations, generated using the true parameters, and assimilate them during five cardiac cycles (i.e., 4 s or 80 000 time-steps).

	DLR			FOM		DLR			FOM
	$R = 10$	$R = 15$	$R = 20$			$R = 10$	$R = 15$	$R = 20$	
SENKF	0.003	0.004	0.003	0.002		0.034	0.028	0.019	0.008
VENKF	0.001	0.001	0.001	0.001		0.027	0.030	0.027	0.010
DENKF	0.001	0.002	0.001	0.001		0.047	0.031	0.023	0.011

(a) β_1 (b) β_{13} Table 4: Relative error $\|\mathbb{E}_P[\hat{\theta}_T] - \theta^{\text{true}}\|/\|\theta^{\text{true}}\|$ (averaged over 3 runs)

	DLR			FOM
	$R = 10$	$R = 15$	$R = 20$	
SENKF	164.9	183.2	208.4	227.8
VENKF	164.0	182.5	206.4	233.1
DENKF	165.5	182.1	206.3	231.6

Table 5: Timings [min]

Figure 9 shows the parameter identification achieved by the SENKF (the results for the VENKF and DENKF are similar). The filter correctly identifies β_1 , while there is more uncertainty for β_{13} due to the limited number of measurements. Similarly, Figures 10, 11 and 12 display the parameter identification achieved by the DLR-SENKF for ranks $R \in \{10, 15, 20\}$. We observe that $R = 20$ correctly capture the filtering density over time, while for $R = 10$, the estimate of β_{13} is biased and the variance is underestimated. Table 4 reports the relative error of the different methods. For β_1 , the DLR-ENKF versions achieve the same level of accuracy as their full-order ENKF counterparts even with small ranks; while for β_{13} , the error tends to decrease as the rank increases. Moreover, Table 5 shows the runtime of the different methods. The DLR versions are faster than their full-order counterparts, and the computational cost increases with the rank. In particular, this runtime could be further improved, since the boundary conditions are solved here at all boundary nodes, even if they are not required to update the solution at the nodes selected by the DEIM algorithm. Finally, Figures 13 and 14 compares the reference flow rate and pressure in the ascending aorta (n°1) and aortic arch I (n°13) with the estimates obtained from the SENKF and the DLR-SENKF with $R = 10$. Both methods accurately recover the flow rate and pressure in each artery after one cardiac cycle.

5 Conclusion

In this work, we have proposed a Dynamical Low-Rank Ensemble Kalman Filter (DLR-ENKF) for joint state-parameter estimation with time-continuous observations. The idea is to constrain the state ensemble to evolve in a low-dimensional subspace that adapts over time, while using an ENKF-type update to correct the augmented state. To this end, we propagate a low-rank approximation of the ensemble through the forecast and analysis steps: the forecast relies on a robust dynamical low-rank integrator inspired by the BUG scheme, while the analysis performs an ENKF-type update that exploits the resulting low-rank structure. To efficiently handle nonlinearities, we further incorporate a DEIM/CUR hyper-reduction method, which evaluates the nonlinear terms only on a small set of selected rows and columns.

The proposed method has been evaluated on the Fisher-KPP equation and on a 1D hyperbolic blood flow model. The numerical experiments show that, for sufficiently large ranks R , the DLR-ENKF achieves an accuracy level comparable to that of its full-order ENKF counterpart, while reducing the computational cost. The results also highlight the

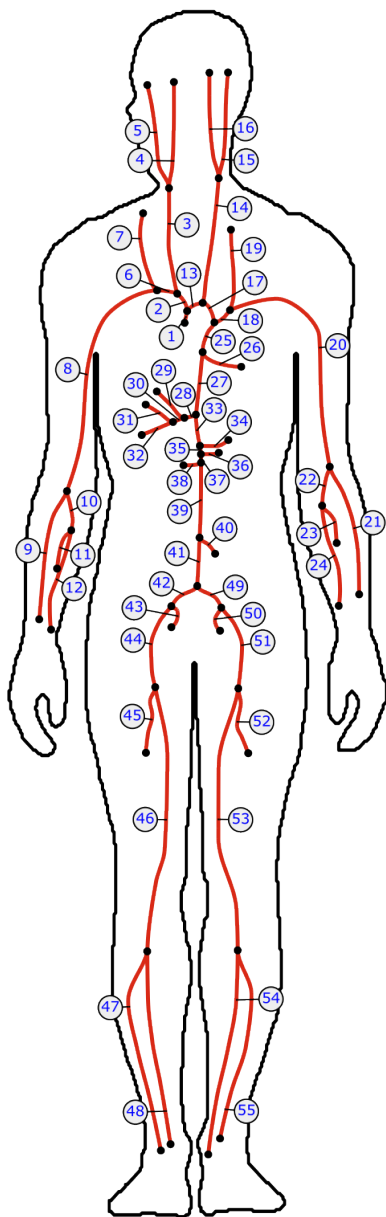


Figure 8: Arterial tree consisting of the 55 main human arteries

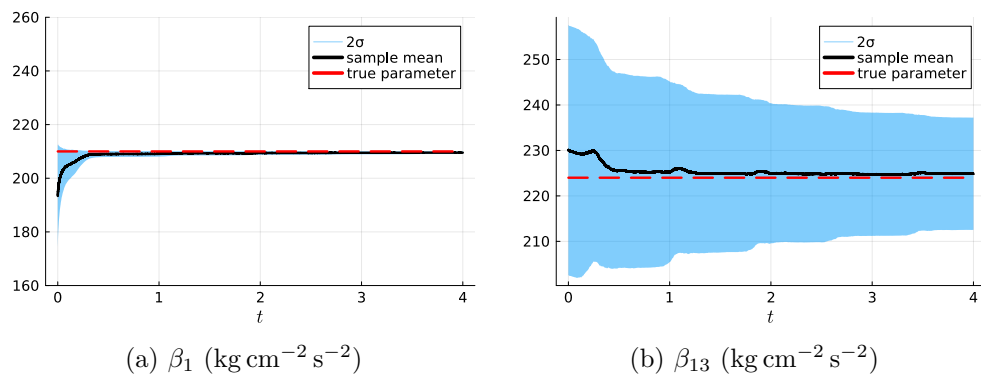


Figure 9: Full Order Model SENKF parameter identification with $P = 100$ particles

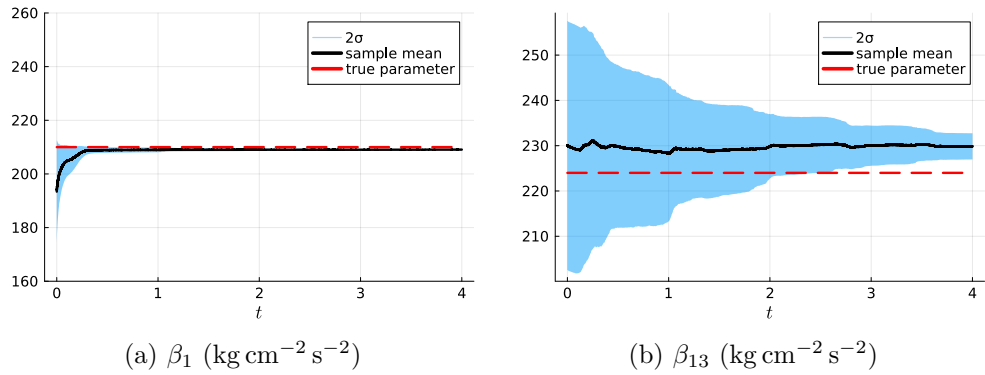


Figure 10: DLR-SENKF ($R = 10$) parameter identification with $P = 100$ particles

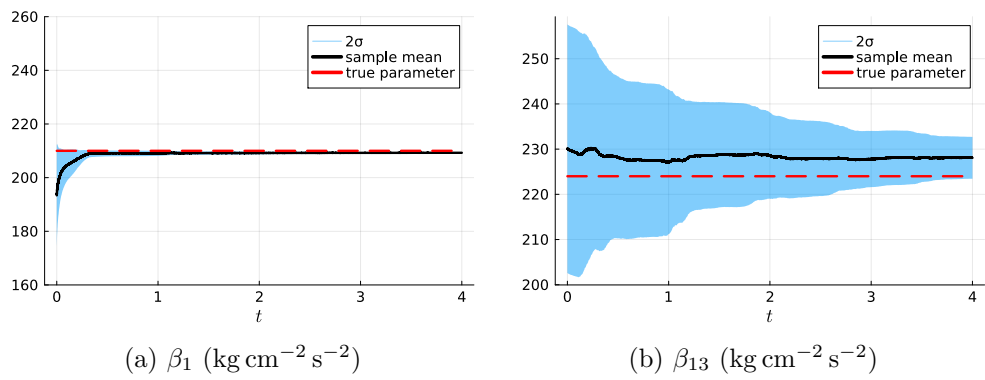


Figure 11: DLR-SENKF ($R = 15$) parameter identification with $P = 100$ particles

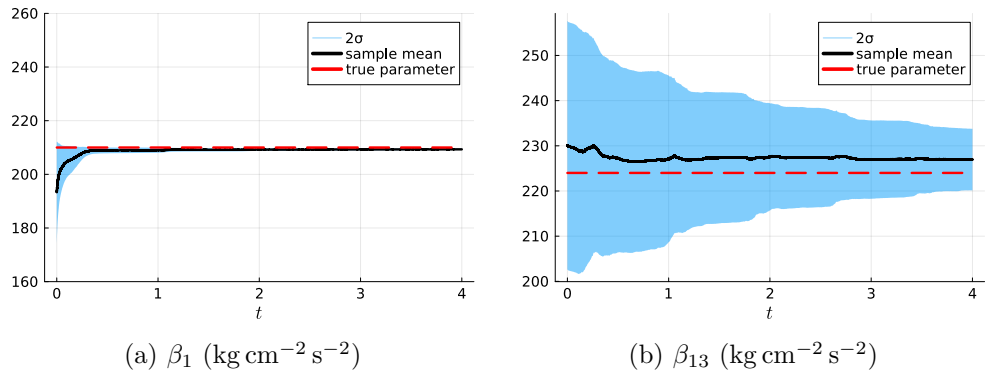


Figure 12: DLR-SENKF ($R = 20$) parameter identification with $P = 100$ particles

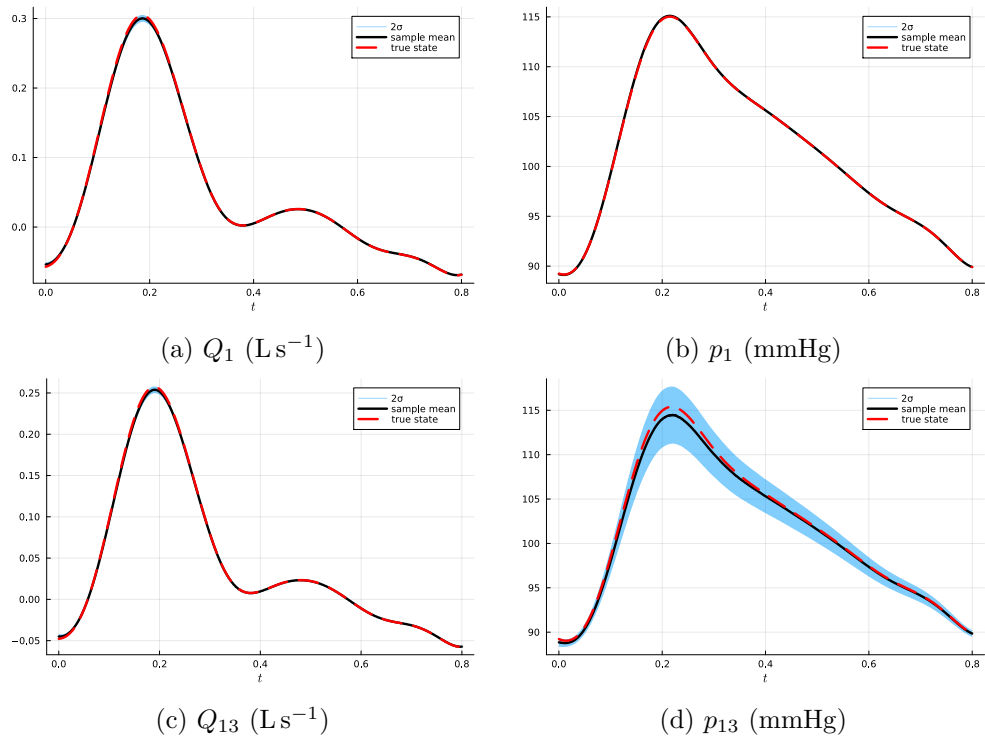


Figure 13: Full Order Model SENKF state estimation with $P = 100$ particles

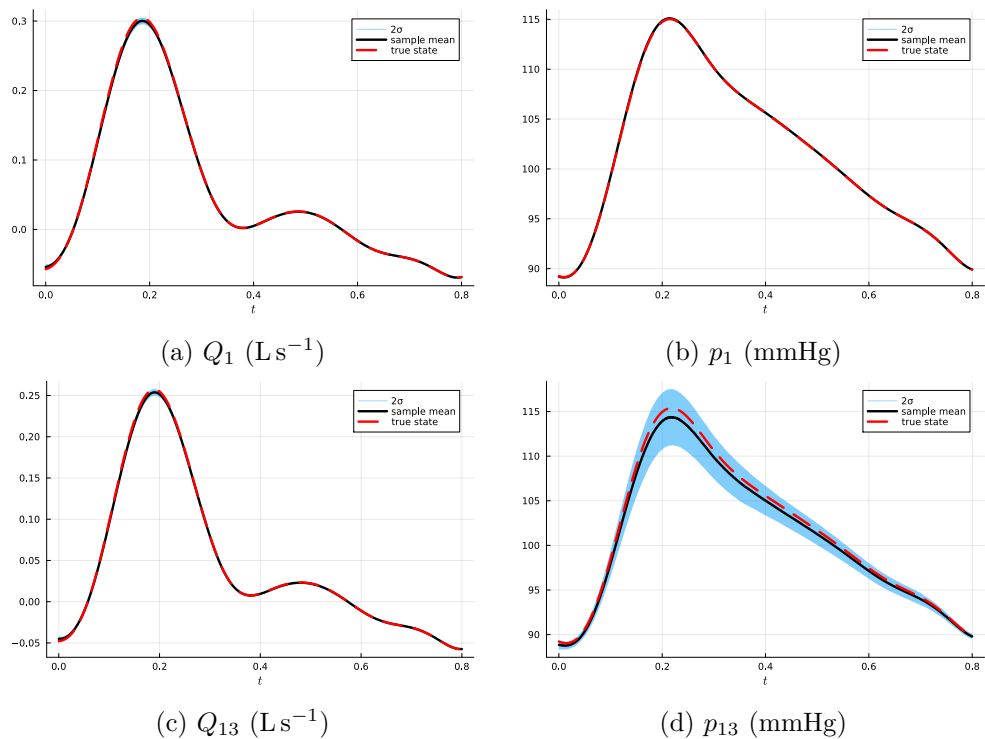


Figure 14: DLR-SENKF ($R = 10$) state estimation with $P = 100$ particles

impact of rank truncation on parameter assimilation and identification: if the rank R is too small, the truncation can lead to biased parameter estimates and an underestimation of the ensemble covariance, especially in partially observed regimes; whereas increasing R tends to improve accuracy towards the full-order level.

In perspective, the computational cost of the DLR-ENKF could be further reduced by using a rank-adaptive strategy that exploits the expected decrease of the rank as the ensemble concentrates, while preventing covariance degeneration. In addition, further speed-ups could be obtained by better integrating the DEIM/CUR method, that is, by ensuring that all computationally expensive terms (e.g., boundary conditions) are evaluated only at the DEIM-selected indices.

Acknowledgements

This work was funded by the Swiss National Science Foundation project “Dynamical low rank methods for uncertainty quantification and data assimilation” (n. 200518).

References

- [1] Jeffrey L. Anderson. An Ensemble Adjustment Kalman Filter for Data Assimilation. *Monthly Weather Review*, 129:2884–2903, 12 2001.
- [2] Maxime Barrault, Yvon Maday, Ngoc Cuong Nguyen, and Anthony T. Patera. An ‘empirical interpolation’ method: application to efficient reduced-basis discretization of partial differential equations. *Comptes Rendus. Mathematique*, 339:667–672, 10 2004.
- [3] Adrian N. Bishop and Pierre Del Moral. On the mathematical theory of ensemble (linear-Gaussian) Kalman–Bucy filtering. *Mathematics of Control, Signals, and Systems*, 35:835–903, 12 2023.
- [4] Dirk Blömker, Claudia Schillings, and Philipp Wacker. A Strongly Convergent Numerical Scheme from Ensemble Kalman Inversion. *SIAM Journal on Numerical Analysis*, 56:2537–2562, 1 2018.
- [5] Gianluca Ceruti, Jonas Kusch, and Christian Lubich. A rank-adaptive robust integrator for dynamical low-rank approximation. *BIT Numerical Mathematics*, 62:1149–1174, 12 2022.
- [6] Gianluca Ceruti and Christian Lubich. An unconventional robust integrator for dynamical low-rank approximation. *BIT Numerical Mathematics*, 62:23–44, 3 2022.
- [7] Saifon Chaturantabut and Danny C. Sorensen. Nonlinear Model Reduction via Discrete Empirical Interpolation. *SIAM Journal on Scientific Computing*, 32:2737–2764, 1 2010.
- [8] P. Del Moral and J. Tugaut. On the stability and the uniform propagation of chaos properties of Ensemble Kalman–Bucy filters. *The Annals of Applied Probability*, 28, 4 2018.
- [9] M. Donello, G. Palkar, M. H. Naderi, D. C. Del Rey Fernández, and H. Babaee. Oblique projection for scalable rank-adaptive reduced-order modelling of nonlinear stochastic partial differential equations with time-dependent bases. *Proceedings of the Royal Society A: Mathematical, Physical and Engineering Sciences*, 479, 10 2023.
- [10] Geir Evensen. Sequential data assimilation with a nonlinear quasi-geostrophic model using Monte Carlo methods to forecast error statistics. *Journal of Geophysical Research: Oceans*, 99:10143–10162, 5 1994.
- [11] Luca Formaggia, Alessandro Veneziani, and Alfio Quarteroni. *Cardiovascular Mathematics - Modeling and simulation of the circulatory system*. Springer-Verlag Milan, 2009.
- [12] Cory D. Hauck and Stefan Schnake. A Predictor-Corrector Strategy for Adaptivity in Dynamical Low-Rank Approximations. *SIAM Journal on Matrix Analysis and Applications*, 44:971–1005, 9 2023.

- [13] Martin Hairer, Arnulf Jentzen, and Peter E Kloeden. Strong and weak divergence in finite time of Euler's method for stochastic differential equations with non-globally Lipschitz continuous coefficients. *Proceedings of the Royal Society A: Mathematical, Physical and Engineering Sciences*, 467(2130):1563–1576, 2011.
- [14] Marco A Iglesias, Kody J H Law, and Andrew M Stuart. Ensemble Kalman methods for inverse problems. *Inverse Problems*, 29:045001, 4 2013.
- [15] Yoshihito Kazashi, Fabio Nobile, and Eva Vidličková. Stability properties of a projector-splitting scheme for dynamical low rank approximation of random parabolic equations. *Numerische Mathematik*, 149:973–1024, 12 2021.
- [16] Yoshihito Kazashi, Fabio Nobile, and Fabio Zoccolan. Dynamical low-rank approximation for stochastic differential equations. *Mathematics of Computation*, 94(333):1335–1375, Aug 2025.
- [17] D.T.B Kelly, K.J.H Law, and A.M. Stuart. Well-posedness and accuracy of the ensemble Kalman filter in discrete and continuous time. *Nonlinearity*, 27:2579–2603, 10 2014.
- [18] Peter E. Kloeden and Eckhard Platen. *Numerical Solution of Stochastic Differential Equations*. Springer Berlin Heidelberg, 1992.
- [19] Othmar Koch and Christian Lubich. Dynamical Low-Rank Approximation. *SIAM Journal on Matrix Analysis and Applications*, 29:434–454, 1 2007.
- [20] Theresa Lange and Wilhelm Stannat. On the continuous time limit of ensemble square root filters. *arXiv preprint arXiv:1910.12493*, 2019.
- [21] Kody Law, Andrew Stuart, and Konstantinos Zygalakis. *Data Assimilation*. Springer International Publishing, 2015.
- [22] Randall J. LeVeque. *Numerical Methods for Conservation Laws*. Birkhäuser Basel, 1992.
- [23] F.Y. Liang, S. Takagi, R. Himeno, and H. Liu. Biomechanical characterization of ventricular–arterial coupling during aging: A multi-scale model study. *Journal of Biomechanics*, 42:692–704, 4 2009.
- [24] D. Lombardi. Inverse problems in 1D hemodynamics on systemic networks: A sequential approach. *International Journal for Numerical Methods in Biomedical Engineering*, 30:160–179, 2 2014.
- [25] Christian Lubich and Ivan V. Oseledets. A projector-splitting integrator for dynamical low-rank approximation. *BIT Numerical Mathematics*, 54:171–188, 3 2014.
- [26] Andrew J. Majda, Di Qi, and Themistoklis P. Sapsis. Blended particle filters for large-dimensional chaotic dynamical systems. *Proceedings of the National Academy of Sciences*, 111:7511–7516, 5 2014.
- [27] Eleonora Musharbash, Fabio Nobile, and Tao Zhou. Error Analysis of the Dynamically Orthogonal Approximation of Time Dependent Random PDEs. *SIAM Journal on Scientific Computing*, 37:A776–A810, 1 2015.
- [28] Fabio Nobile and Sébastien Riffaud. Robust high-order low-rank BUG integrators based on explicit Runge-Kutta methods. *arXiv preprint arXiv:2502.07040*, Feb 2025.
- [29] Fabio Nobile and Thomas Trigo Trindade. Dynamical Low-Rank Approximations for Kalman Filtering. *arXiv preprint arXiv:2509.11210*, Sep 2025.
- [30] Nikolas Nüsken, Sebastian Reich, and Paul J. Rozdeba. State and Parameter Estimation from Observed Signal Increments. *Entropy*, 21:505, 5 2019.
- [31] Stefano Pagani, Andrea Manzoni, and Alfio Quarteroni. Efficient State/Parameter Estimation in Nonlinear Unsteady PDEs by a Reduced Basis Ensemble Kalman Filter. *SIAM/ASA Journal on Uncertainty Quantification*, 5:890–921, 1 2017.
- [32] Sébastien Riffaud, Miguel A. Fernández, and Damiano Lombardi. A Low-Rank Solver for Parameter Estimation and Uncertainty Quantification in Time-Dependent Systems of Partial Differential Equations. *Journal of Scientific Computing*, 99:34, 5 2024.
- [33] Daniel Sanz-Alonso, Andrew Stuart, and Armeen Taeb. *Inverse Problems and Data Assimilation*. Cambridge University Press, 7 2023.

- [34] Themistoklis P. Sapsis and Pierre F.J. Lermusiaux. Dynamically orthogonal field equations for continuous stochastic dynamical systems. *Physica D: Nonlinear Phenomena*, 238:2347–2360, 12 2009.
- [35] Themistoklis P. Sapsis and Andrew J. Majda. A statistically accurate modified quasi-linear Gaussian closure for uncertainty quantification in turbulent dynamical systems. *Physica D: Nonlinear Phenomena*, 252:34–45, 6 2013.
- [36] Themistoklis P. Sapsis and Andrew J. Majda. Blended reduced subspace algorithms for uncertainty quantification of quadratic systems with a stable mean state. *Physica D: Nonlinear Phenomena*, 258:61–76, 9 2013.
- [37] Claudia Schillings and Andrew M. Stuart. Analysis of the Ensemble Kalman Filter for Inverse Problems. *SIAM Journal on Numerical Analysis*, 55:1264–1290, 1 2017.
- [38] Francesco A. B. Silva, Cecilia Pagliantini, Martin Grepl, and Karen Veroy. A reduced basis ensemble Kalman method. *GEM - International Journal on Geomathematics*, 14, 12 2023.
- [39] Francesco A. B. Silva, Cecilia Pagliantini, and Karen Veroy. An Adaptive Hierarchical Ensemble Kalman Filter with Reduced Basis Models. *SIAM/ASA Journal on Uncertainty Quantification*, 13:140–170, 3 2025.
- [40] Thomas Sondergaard and Pierre F. J. Lermusiaux. Data Assimilation with Gaussian Mixture Models Using the Dynamically Orthogonal Field Equations. Part I: Theory and Scheme. *Monthly Weather Review*, 141:1737–1760, 6 2013.
- [41] Thomas Sondergaard and Pierre F. J. Lermusiaux. Data Assimilation with Gaussian Mixture Models Using the Dynamically Orthogonal Field Equations. Part II: Applications. *Monthly Weather Review*, 141:1761–1785, 6 2013.
- [42] Bram van Leer. Towards the ultimate conservative difference scheme. V. A second-order sequel to Godunov's method. *Journal of Computational Physics*, 32:101–136, 7 1979.
- [43] Jeffrey S. Whitaker and Thomas M. Hamill. Ensemble Data Assimilation without Perturbed Observations. *Monthly Weather Review*, 130:1913–1924, 7 2002.

No.	Artery	Length (m)	A_0 (m 2)	β (kg m $^{-2}$ s $^{-2}$)
1	Ascending Aorta	2.0×10^{-2}	6.812×10^{-4}	210×10^4
2	Brachiocephalic	3.4×10^{-2}	1.267×10^{-4}	652×10^4
3	R. Carotid	17.6×10^{-2}	0.466×10^{-4}	1079×10^4
4	R. Internal Carotid	17.6×10^{-2}	0.26×10^{-4}	2324×10^4
5	R. External Carotid	17.6×10^{-2}	0.126×10^{-4}	4042×10^4
6	R. Subclavian I	3.4×10^{-2}	0.544×10^{-4}	797×10^4
7	R. Vertebral	13.4×10^{-2}	0.126×10^{-4}	5505×10^4
8	R. Subclavian II	39.8×10^{-2}	0.319×10^{-4}	1077×10^4
9	R. Radial	22.0×10^{-2}	0.078×10^{-4}	7704×10^4
10	R. Ulnar I	6.6×10^{-2}	0.145×10^{-4}	4248×10^4
11	R. Interosseous	7.0×10^{-2}	0.031×10^{-4}	28722×10^4
12	R. Ulnar II	17.0×10^{-2}	0.115×10^{-4}	9714×10^4
13	Aortic Arch I	3.0×10^{-2}	5.992×10^{-4}	224×10^4
14	L. Carotid	20.8×10^{-2}	0.466×10^{-4}	1079×10^4
15	L. External Carotid	17.6×10^{-2}	0.126×10^{-4}	4042×10^4
16	L. Internal Carotid	17.6×10^{-2}	0.26×10^{-4}	2324×10^4
17	Aortic Arch II	4.0×10^{-2}	5.26×10^{-4}	239×10^4
18	L. Subclavian I	3.4×10^{-2}	0.544×10^{-4}	797×10^4
19	L. Vertebral	13.4×10^{-2}	0.126×10^{-4}	5505×10^4
20	L. Subclavian II	39.8×10^{-2}	0.319×10^{-4}	1077×10^4
21	L. Radial	22.0×10^{-2}	0.078×10^{-4}	7704×10^4
22	L. Ulnar I	6.6×10^{-2}	0.145×10^{-4}	4248×10^4
23	L. Interosseous	7.0×10^{-2}	0.031×10^{-4}	28722×10^4
24	L. Ulnar II	17.0×10^{-2}	0.115×10^{-4}	9714×10^4
25	Thoracic Aorta I	5.4×10^{-2}	4.412×10^{-4}	261×10^4
26	Intercostals	7.2×10^{-2}	0.283×10^{-4}	2008×10^4
27	Thoracic Aorta II	10.4×10^{-2}	3.294×10^{-4}	302×10^4
28	Celiac I	2.0×10^{-2}	0.332×10^{-4}	1252×10^4
29	Hepatic	6.4×10^{-2}	0.216×10^{-4}	2124×10^4
30	Celiac II	2.0×10^{-2}	0.238×10^{-4}	1843×10^4
31	Gastric	5.4×10^{-2}	0.126×10^{-4}	2426×10^4
32	Splenic	5.8×10^{-2}	0.083×10^{-4}	3801×10^4
33	Abdominal Aorta I	5.2×10^{-2}	2.438×10^{-4}	351×10^4
34	Superior Mesenteric	5.0×10^{-2}	0.442×10^{-4}	1052×10^4
35	Abdominal Aorta II	1.4×10^{-2}	2.143×10^{-4}	375×10^4
36	L. Renal	3.0×10^{-2}	0.238×10^{-4}	1577×10^4
37	Abdominal Aorta III	1.5×10^{-2}	2.026×10^{-4}	385×10^4
38	R. Renal	3.0×10^{-2}	0.238×10^{-4}	1577×10^4
39	Abdominal Aorta IV	12.4×10^{-2}	1.581×10^{-4}	436×10^4
40	Inferior Mesenteric	3.8×10^{-2}	0.11×10^{-4}	2468×10^4
41	Abdominal Aorta V	8.0×10^{-2}	1.088×10^{-4}	526×10^4
42	R. Common Iliac	5.8×10^{-2}	0.466×10^{-4}	931×10^4
43	R. Internal Iliac	4.4×10^{-2}	0.126×10^{-4}	6043×10^4
44	R. External Iliac	14.4×10^{-2}	0.367×10^{-4}	1722×10^4
45	R. Deep Femoral	11.2×10^{-2}	0.126×10^{-4}	3678×10^4
46	R. Femoral	44.2×10^{-2}	0.272×10^{-4}	2640×10^4
47	R. Posterior Tibial	34.4×10^{-2}	0.096×10^{-4}	9717×10^4
48	R. Anterior Tibial	32.2×10^{-2}	0.196×10^{-4}	4533×10^4
49	L. Common Iliac	5.8×10^{-2}	0.466×10^{-4}	931×10^4
50	L. Internal Iliac	4.4×10^{-2}	0.126×10^{-4}	6043×10^4
51	L. External Iliac	14.4×10^{-2}	0.367×10^{-4}	1722×10^4
52	L. Deep Femoral	11.2×10^{-2}	0.126×10^{-4}	3678×10^4
53	L. Femoral	44.2×10^{-2}	0.272×10^{-4}	2640×10^4
54	L. Anterior Tibial	34.4×10^{-2}	0.196×10^{-4}	4533×10^4
55	L. Posterior Tibial	32.2×10^{-2}	0.096×10^{-4}	9717×10^4

Table 6: Physiological properties of the arterial tree. The data are taken and adapted from [23]